Advances in Water Resources 161 (2022) 104129

Contents lists available at ScienceDirect

Advances in Water Resources

journal homepage: www.elsevier.com/locate/advwatres

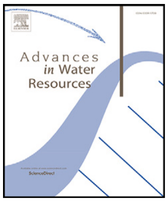

A hybrid-mixed finite element method for single-phase Darcy flow in fractured porous media

Guosheng Fu [a,1], Yang Yang [b,*,2]

[a] Department of Applied and Computational Mathematics and Statistics, University of Notre Dame, USA
[b] Department of Mathematical Sciences, Michigan Technological University, USA

ARTICLE INFO

MSC:
65N30
65N12
76S05
76D07

Keywords:
Hybrid-mixed finite element method
Fractured porous media
Hybrid-dimensional model

ABSTRACT

We present a hybrid-mixed finite element method for a novel hybrid-dimensional model of single-phase Darcy flow in a fractured porous media. In this model, the fracture is treated as a $(d-1)$-dimensional interface within the d-dimensional fractured porous domain, for $d = 2, 3$. Two classes of fracture are distinguished based on the permeability magnitude ratio between the fracture and its surrounding medium: when the permeability in the fracture is (significantly) larger than in its surrounding medium, it is considered as a *conductive* fracture; when the permeability in the fracture is (significantly) smaller than in its surrounding medium, it is considered as a *blocking* fracture. The conductive fractures are treated using the classical hybrid-dimensional approach of the interface model where pressure is assumed to be continuous across the fracture interfaces, while the blocking fractures are treated using the recent Dirac-δ function approach where normal component of Darcy velocity is assumed to be continuous across the interface. Due to the use of Dirac-δ function approach for the blocking fractures, our numerical scheme allows for nonconforming meshes with respect to the blocking fractures. This is the major novelty of our model and numerical discretization. Moreover, our numerical scheme produces locally conservative velocity approximations and leads to a symmetric positive definite linear system involving pressure degrees of freedom on the mesh skeleton only. As an application, we extend the idea to a simple transport model. The performance of the proposed method is demonstrated by various benchmark test cases in both two- and three-dimensions. Numerical results indicate that the proposed scheme is highly competitive with existing methods in the literature

1. Introduction

Numerical simulations of single- and multi-phase flows in porous media have many applications in contaminant transportation, oil recovery and underground radioactive waste deposit. Due to the highly conductive and blocking fractures in the porous media underground, it is still challenging to construct accurate numerical approximations (Matthäi et al., 2010; Vasilyeva et al., 2019; Golian et al., 2020).

There are several commonly used mathematical models for simulating flows in porous media with conductive fractures, such as the dual porosity model (Barenblatt et al., 1960; Warren and Root, 1963; Geiger et al., 2013), single porosity model (Ghorayeb and Firoozabadi, 2000), traditional discrete fracture model (DFM) (Noorishad and Mehran, 1982; Baca et al., 1984; Kim and Deo, 1999, January, 2000; Karimi-Fard and Firoozabadi, 2001; Geiger-Boschung et al., 2009; Zhang et al., 2013), embedded DFM (EDFM) (Li and Lee, 2008; Moinfar, 2013; Yan et al., 2016; Tene et al., 2017; Jiang and Younis, 2017a; HosseiniMehr et al., 2018; Xu et al., 2019), the interface models (Alboin et al., 1999, 2000; Hansbo and Hansbo, 2002; Odsæter et al., 2019) and extended finite element DFM (XDFM) based on the interface models (Fumagalli and Scotti, 2014; Huang et al., 2011; Schwenck, 2015; Salimzadeh and Khalili, 2015; Flemisch et al., 2016), finite element method based on Lagrange multipliers (Köppel et al., 2019a,b; Schädle et al., 2019), etc. Among the above methods, the traditional DFM and the interface models have been intensively studied in the past decades.

The DFM is based on the principle of superposition. It uses a hybrid dimensional representation of the Darcy's law, and treats the fractures as lower dimensional entries, with the thickness of the fracture as the dimensional homogeneity factor. The first DFM was introduced by Noorishad and Mehran (1982) in 1982 for single phase flows. Later, Baca et al. (1984) considered the heat and solute transport in fractured media. Subsequently, several significant numerical methods were applied to the DFM, such as the finite element methods (Kim

---

[*] Corresponding author.
E-mail addresses: gfu@nd.edu (G. Fu), yyang7@mtu.edu (Y. Yang).
[1] G. Fu was partially supported by the NSF grant DMS-2012031.
[2] Y. Yang was partially supported by the NSF grant DMS-1818467.

https://doi.org/10.1016/j.advwatres.2022.104129
Received 7 September 2021; Received in revised form 13 January 2022; Accepted 18 January 2022

and Deo, 1999, January, 2000; Karimi-Fard and Firoozabadi, 2001; Geiger-Boschung et al., 2009; Zhang et al., 2013), vertex-centered finite volume methods (Monteagudo and Firoozabadi, 2004; Reichenberger et al., 2006; Monteagudo and Firoozabadi, 2007; Zhang et al., 2016), cell-centered finite volume methods (Karimi-Fard et al., 2003; Sandve et al., 2012; Ahmed et al., 2015; Gl"aser et al., 2017; Fang et al., 2018), mixed finite element methods (Hoteit and Firoozabadi, 2005, 2006, 2008b,a; Moortgat and Firoozabadi, 2013a,b; Zidane and Firoozabadi, 2014; Moortgat et al., 2016), discontinuous Galerkin methods (Antonietti et al., 2019). All the above works are limited on conforming meshes, i.e. the fractures are aligned with the interfaces of the background matrix cells. Therefore, it may suffer from low quality cells. Recently, Xu and Yang introduced the Dirac-δ functions (Xu and Yang, 2020) to represent the conductive fractures and reinterpreted the DFM (RDFM) on nonconforming meshes. The basic idea is to superpose the conductivity of the fracture to that of the matrix. The main contribution in Xu and Yang (2020) is to explicitly represent the DFM introduced in Karimi-Fard and Firoozabadi (2001) as a scalar partial differential equation. Therefore, with suitable numerical discretizations, such as the discontinuous Galerkin method, the RDFM can be applied to arbitrary meshes. To demonstrate that the RDFM is exactly the traditional DFM if the mesh is conforming, in Xu and Yang (2020) only finite element methods were considered. Therefore, local mass conservation was missing. Later, the enriched Galerkin and interior penalty discontinuous Galerkin methods were applied to RDFM in Feng et al. (2021) and the contaminant transportation was also simulated.

Different from the traditional DFM, the interface model (Alboin et al., 1999, 2000; Hansbo and Hansbo, 2002; Odsæter et al., 2019) explicitly represent the fractures as interfaces of the porous media. Then the governing equation of the flow in the lower dimensional fracture was constructed. In the interface model, the matrix and fractures are considered as two systems, and the communication between them was given as the jump of the normal velocity along the fractures. Therefore, different from RDFM, the interface model, though hanging nodes are allowable, cannot be applied to structured meshes and the fracture must be aligned with the interfaces of the meshes for the matrix. To fixed this limitation, the XDFM was proposed (Fumagalli and Scotti, 2014; Huang et al., 2011; Schwenck, 2015; Salimzadeh and Khalili, 2015; Flemisch et al., 2016). However, these methods may increase the degrees of freedom (DOFs) significantly, and can hardly be applied to fracture networks with high geometrical complexity (Flemisch et al., 2018). As an alternative, the CutFEM (Burman et al., 2019) can be applied to non-conforming meshes. It couples the fluid flow in all lower dimensional manifolds. However, this method requires the fractures to cut the domain into completely disjoint subdomains, thus it is not applicable for media with complicated fractures.

Most of the above ideas work for problems with conductive fractures. However, if the media contains blocking fractures, most methods may not be suitable. To fix this gap, the projection-based EDFM (pEDFM) was introduced in Tene et al. (2017) and Jiang and Younis (2017b). The effective flow area between adjacent matrix grids is computed as the difference between the original interface area and the projected area of the fracture segment. It will be zero if the fracture fully penetrates through the matrix cell. Olorode et al. (2020) extended the pEDFM into three-dimensional compositional simulation of fractured reservoirs. However the pEDFM still cannot describe the complex multiphase flow behavior in the matrix blocks within barrier fractures. Another approach is to follow the interface model introduced in Martin et al. (2005), Angot et al. (2009), Boon et al. (2018) and Kadeethum et al. (2020). However, as demonstrated above, the interface model can only handle hanging nodes, and the fractures must align with the interfaces of the background mesh. Recently, Xu and Yang extended the RDFM (Xu and Yang, 2020; Feng et al., 2021) to problems with blocking fractures in Xu et al. (2021). The basic idea is to apply Ohm's law and superpose the resistance (the reciprocal of the permeability) of the blocking fracture to that of the matrix. Then a modified partial differential equation system was introduced and the local discontinuous Galerkin methods with suitable penalty were perfectly applied. If the problems contains only blocking fractures, the mixed finite element methods can easily be combined with RDFM.

In this paper, we combine the ideas in Alboin et al. (1999) and Xu et al. (2021) to propose a novel model for single phase flows in porous media. The idea works for problems containing both conductive and blocking fractures. In particular, the interface model (Alboin et al., 1999) was used to enforce the continuity of pressure across the conductive fractures, while the Dirac-δ functions were applied for the blocking fractures to superpose the resistance following the main idea given in Xu et al. (2021). The separate treatment of conductive and blocking fractures may yield difficulties in constructing mathematical models. Therefore, one of the major novelty of the current work is the seamless combination of the conductive fracture interface model and the blocking fracture Dirac-δ function approach. With the new mathematical model, we further construct numerical discretization by using a hybrid-mixed finite element method. The proposed method has the following features: (1) it produces locally conservative velocity approximations; (2) it leads to a symmetric positive definite linear system; (3) it only produces globally coupled degrees of freedom (DOFs) of pressure on the mesh skeletons. Therefore, the numerical scheme yields much less total DOFs and is easy to implement, and this is the main advantage compared with the XDFM, pEDFM and CutFEM methods. Moreover, thanks to the Dirac-δ functions for blocking fractures, the method does not require any mesh conformity with respect to the blocking fractures, which is another major novelty of our proposed scheme compared with the interface model. To the best knowledge of the authors, our approach is the simplest one that can be applied to non-conforming mesh for blocking fractures that still yield locally conservative velocity approximations. We note that mesh conformity with respect to the conductive fractures is still required for our method, which is typical for interface models. We numerically demonstrate that our hybrid-mixed finite element scheme is highly competitive both in terms of computational efficiency and accuracy. As an application, we couple the proposed flow equation with the simple transport equations and construct the locally conservative hybrid finite volume methods for the transport equations. We finally emphasis that the proposed hybrid-mixed formulation is different from the mixed method in Boon et al. (2018) due to the use of different model for the interface conditions. We believe that our model is significantly simpler for complex fracture networks since we only use one matrix domain and one (codimension 1) conductive fracture domain throughout, while the mixed method formulation (Boon et al., 2018) needs to split the matrix and fracture domains into multiple disjoint sub-domains and require the modeling of codimension 1–3 fracture flows, which might be very tedious to perform for complex fracture networks.

The rest of the paper is organized as follows. In Section 2, we present the hybrid-dimensional model under consideration. We then formulate in Section 3 the hybrid-mixed finite element discretization of the model proposed in Section 2. Numerical results for various benchmark test cases are presented in Section 4. We conclude in Section 5.

2. The hybrid-dimensional model

2.1. Notation

We consider a bounded open domain $\Omega_m \subset \mathbb{R}^d$, $d = 2, 3$, which contains several $(d-1)$-dimensional conductive or blocking fractures. For simplicity, the fractures are assumed to be hyperplanes with smooth boundaries. We denote Ω_c as the $(d-1)$-dimensional open set containing all the conductive fractures, and Ω_b as the set containing all the blocking fractures. Assume the $(d-1)$-dimensional domain boundary $\partial\Omega_m = \Gamma_D \cup \Gamma_N$, with $\Gamma_D \cap \Gamma_N = \emptyset$. Furthermore, we denote the following sets of $(d-2)$-dimensional boundaries (intersections) associated with the set of conductive fractures Ω_c:

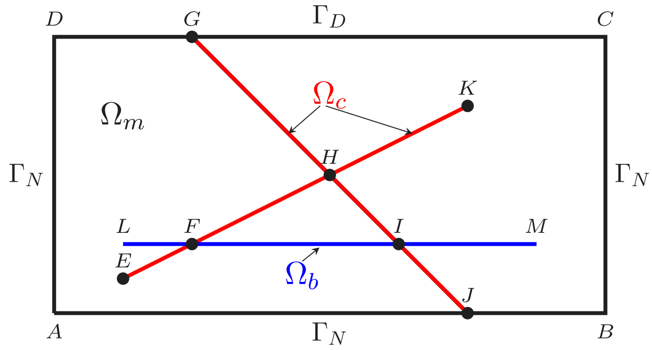

Fig. 1. A typical two dimensional fractured domain Ω_m (the rectangular domain). The domain boundary $\Gamma_D = \{CD\}$, $\Gamma_N = \{AB\}\cup\{BC\}\cup\{AD\}$, where $\{AB\}$ denotes the line segment connecting nodes A and B. Here $\Omega_c = \{EK\}\cup\{JG\}$, $\Omega_b = \{LM\}$, $\Gamma_{cc} = H$, $\Gamma_{cb} = F\cup I$, $\Gamma_{cm}^D = G$, $\Gamma_{cm}^N = J$, and $\Gamma_{ci} = E\cup K$.

- Γ_{cc} is the set containing the intersections among conductive fractures.
- Γ_{cb} is the set containing the intersections between 2 conductive and blocking fractures.
- Γ_{cm} is the set containing the intersections between conductive fractures and domain boundary $\partial\Omega_m$, which is further split to $\Gamma_{cm} = \Gamma_{cm}^N \cup \Gamma_{cm}^D$ with $\Gamma_{cm}^N \in \Gamma_N$ and $\Gamma_{cm}^D \in \Gamma_D$.
- Γ_{ci} is the boundary of Ω_c that does not intersect with the domain boundary $\partial\Omega_m$.

We set $\Gamma_c = \Gamma_{cc}\cup\Gamma_{cb}\cup\Gamma_{cm}\cup\Gamma_{ci}$ as the collections of all intersections of Ω_c. An illustration of a typical hybrid-dimensional domain in two-dimensions is given in Fig. 1.

We denote $\boldsymbol{n}_\Gamma$ as a uniquely oriented unit normal vector on a $(d-1)$-dimensional interface/boundary Γ, and denote $\boldsymbol{\eta}_\Gamma$ as the *in-plane* unit (outer) normal vector on the $(d-2)$ dimensional boundary $\partial\Gamma$ of Γ, see Fig. 2.

Let ϵ be the thickness of the fractures, which is assumed to be a small positive constant for simplicity. Let $\mathbb{K}_m$ be the permeability tensor of the domain excluding the fractures $\Omega_m\backslash\{\Omega_c\cup\Omega_b\}$, $K_b \ll \mathbb{K}_m$ be the (scalar) permeability in the normal direction of blocking fractures Ω_b, and $\mathbb{K}_c \gg \mathbb{K}_m$ be the permeability tensor in the tangential direction of the conductive fractures Ω_c.

2.2. The hybrid-dimensional flow model

The following hybrid-dimensional model is a combination of the conductive fracture treatment in Alboin et al. (1999) and blocking fracture treatment in Xu et al. (2021). We apply the Dirac δ-functions in the bulk domain $\Omega_m\backslash\Omega_c$ excluding conductive fractures and the model reads:

$$(\mathbb{K}_m^{-1} + \frac{\epsilon}{K_b}\delta_{\Omega_b}\boldsymbol{n}_{\Omega_b}\otimes\boldsymbol{n}_{\Omega_b})\boldsymbol{u} = -\nabla p, \quad \text{in } \Omega_m\backslash\Omega_c, \tag{1a}$$

$$\nabla\cdot\boldsymbol{u} = f, \quad \text{in } \Omega_m\backslash\Omega_c, \tag{1b}$$

where $\boldsymbol{u}$ is the Darcy velocity, p is the pressure, f is the volume source term, δ_{Ω_b} is the Dirac-δ function that takes values ∞ on the blocking fractures Ω_b and zero elsewhere, and $\boldsymbol{n}_{\Omega_b}$ is the unit normal vector on Ω_b. The basic idea is to superpose the resistance of the porous media to reduce the Darcy velocity in the normal direction of the blocking fractures Within the conductive fractures excluding intersections $\Omega_c\backslash\Gamma_c$, we use the following $(d-1)$-dimensional Darcy's law:

$$(\epsilon\mathbb{K}_c)^{-1}\boldsymbol{u}_c = -\nabla_\Gamma p_c, \quad \text{in } \Omega_c\backslash\Gamma_c, \tag{1c}$$

$$\nabla_\Gamma\cdot\boldsymbol{u}_c = [\![\boldsymbol{u}]\!], \quad \text{in } \Omega_c\backslash\Gamma_c, \tag{1d}$$

where $\boldsymbol{u}_c$ is the (tangential) Darcy velocity in the conductive fractures, p_c is the associated pressure, and the velocity jump $[\![\boldsymbol{u}]\!] = (\boldsymbol{u}^+ - \boldsymbol{u}^-)\cdot\boldsymbol{n}_\Gamma$ represents the mass exchange between the conductive fractures and the surrounding media, where $\boldsymbol{u}^\pm(\boldsymbol{x}) = \lim_{\tau\to 0^\pm}\boldsymbol{u}(\boldsymbol{x}-\tau\boldsymbol{n}_\Gamma)$ for all $\boldsymbol{x}\in\Omega_c$ is the bulk Darcy velocity evaluated on one side of the conductive fractures. Moreover, ∇_Γ and $\nabla_\Gamma\cdot$ are the usual surface gradient and surface divergence operators. The above equations give the modified Darcy's law for flow in porous media containing both conductive and blocking fractures. We close the hybrid-dimensional system with the following set of boundary/interface conditions:

$$p = p_D, \quad \text{on } \Gamma_D, \tag{1e}$$

$$\boldsymbol{u}\cdot\boldsymbol{n} = q_N, \quad \text{on } \Gamma_N, \tag{1f}$$

$$p = p_c, \quad \text{on } \Omega_c, \tag{1g}$$

$$[\![\boldsymbol{u}_c]\!] = 0, \quad \text{on } \Gamma_{cc}, \tag{1h}$$

$$p_c = p_D, \quad \text{on } \Gamma_{cm}^D, \tag{1i}$$

$$\boldsymbol{u}_c\cdot\boldsymbol{\eta}_\Gamma = 0, \quad \text{on } \Gamma_{cb}\cup\Gamma_{cm}^N\cup\Gamma_{ci}, \tag{1j}$$

where (1g) ensures continuity of bulk pressure across conductive fractures, the no-flow boundary condition in (1j) is imposed on the intersections Γ_{cb}, Γ_{cm}^N and Γ_{ci}, and the jump term in (1h) is

$$[\![\boldsymbol{u}_c]\!]\Big|_e := \sum_{\Gamma\subset\Omega_c\backslash\Gamma_c,\, e\in\overline{\Gamma}} \boldsymbol{u}_c|_\Gamma\cdot\boldsymbol{\eta}_\Gamma, \quad \forall e\in\Gamma_{cc},$$

which represents mass conservation along intersections Γ_{cc}. Note in particular that each conductive fracture containing the intersection e appears exactly twice in the above summation, and the in-plane normal velocity on the fracture is allowed to be discontinuous along the intersection e. For example, the jump $[\![\boldsymbol{u}_c]\!]|_H$ at node H in the configuration in Fig. 1 is

$$[\![\boldsymbol{u}_c]\!]|_H := \sum_{\Gamma\in\{\{EH\},\{HK\},\{GH\},\{HJ\}\}} \boldsymbol{u}_c|_\Gamma\cdot\boldsymbol{\eta}_\Gamma.$$

We note that in the above model (1), the flow in the tangential direction in the blocking fractures is completely ignored as the permeability therein is much smaller than that of the surroundings, on the other hand, the flow in the normal direction is ignored on conductive fractures by the pressure continuity condition (1g) since the permeability is much larger than that of the surroundings and the fluid has a tendency to flow along the tangential direction therein.

2.3. The hybrid-dimensional transport model

We now consider a scalar quantity c that is transported through the porous medium subject to the velocity fields in the flow model (1). Here c usually represents the concentration of a generic passive tracer. Similar to the flow treatment in the previous subsection, transport inside the blocking fractures is ignored. The concentrations c in the matrix and c_c in the conductive fractures are governed by the following advection equations, see e.g. (Alboin et al., 2002; Fumagalli and Scotti, 2013; Odsæter et al., 2019),

$$\phi_m\frac{\partial c}{\partial t} + \nabla\cdot(\boldsymbol{u}c) = cf, \quad \text{in } \Omega_m\backslash\Omega_c\times(0,T], \tag{2a}$$

$$\epsilon\phi_c\frac{\partial c_c}{\partial t} + \nabla_\Gamma\cdot(\boldsymbol{u}_c c_c) - [\![c\boldsymbol{u}]\!] = 0, \quad \text{in } \Omega_c\times(0,T], \tag{2b}$$

with the following initial, interface, and boundary conditions

$$c = c_c \quad \text{on } \Omega_c\times(0,T], \tag{2c}$$

$$c = c_0 \quad \text{on } \Omega\times 0, \qquad c_c = c_{c,0} \quad \text{on } \Omega_c\times 0, \tag{2d}$$

$$c = c_B \quad \text{on } \partial\Omega_{in}\times(0,T], \quad c_c = c_{c,B} \quad \text{on } \Gamma_{in}\times(0,T], \tag{2e}$$

where $\{\phi_m, c_0, c_B, \partial\Omega_{in}\}$ and $\{\phi_c, c_{c,0}, c_{c,B}, \Gamma_{in}\}$ represent the {porosity, initial concentration, inflow concentration, and inflow boundary} in the matrix and conductive fractures, respectively. Observe that concentration continuity (2c) across the conductive fractures are enforced in the model (2).

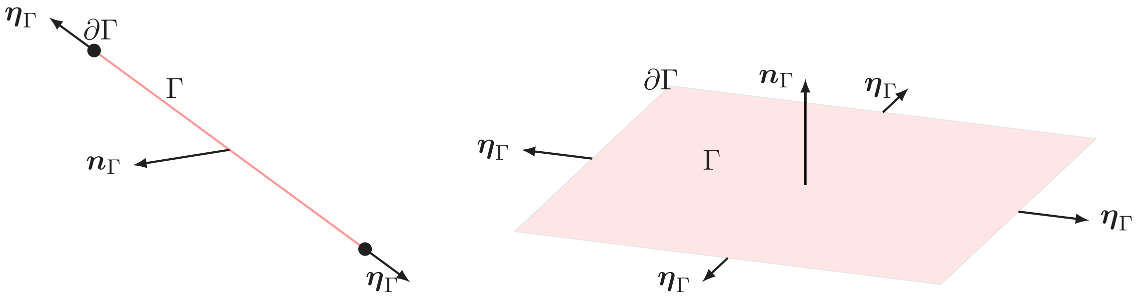

(a) 2D case (b) 3D case

Fig. 2. Normal direction $\boldsymbol{n}_\Gamma$ and in-plane normal direction $\boldsymbol{\eta}_\Gamma$ for a $(d-1)$-dimensional interface/boundary Γ. Left: $d=2$, Γ is a line segment. Right: $d=3$, Γ is a planar quadrangle.

3. The hybrid-mixed finite element method

3.1. Preliminaries

Let $\mathcal{T}_h := \{K\}$ be a conforming simplicial triangulation of the domain Ω_m. Let $\mathcal{E}_h$ be the collections of $(d-1)$-dimensional facets (edges for $d=2$, faces for $d=3$) of Ω_m. Assume the mesh is fully fitted with respect to the conductive fractures, i.e., $\mathcal{T}_h^c := \Omega_c \cap \mathcal{E}_h$ is a $(d-1)$-dimensional simplicial triangulation of the domain Ω_c. Here the mesh $\mathcal{T}_h$ is allowed to be unfitted with respect to the blocking fractures. Moreover, we denote $\mathcal{E}_h^c$ as the collection of $(d-2)$-dimensional facets of $\mathcal{T}_h^c$ (vertices for $d=2$, edges for $d=3$).

We use the lowest-order hybrid-mixed finite element methods to discretize the model (1). The following finite element spaces will be needed:

$$\boldsymbol{V}_h := \{\boldsymbol{v} \in [L^2(\mathcal{T}_h)]^d \,:\, \boldsymbol{v}|_K \in RT_0(K), \quad \forall K \in \mathcal{T}_h\}, \tag{3a}$$

$$W_h := \{w \in L^2(\mathcal{T}_h) \,:\, w|_K \in P_0(K), \quad \forall K \in \mathcal{T}_h\}, \tag{3b}$$

$$M_h := \{\mu \in L^2(\mathcal{E}_h) \,:\, \mu|_F \in P_0(F), \quad \forall F \in \mathcal{E}_h\}, \tag{3c}$$

$$\boldsymbol{V}_h^c := \{\boldsymbol{v}_c \in [L^2(\mathcal{T}_h^c)]^d \,:\, \boldsymbol{v}|_F \in RT_0(F), \quad \forall F \in \mathcal{T}_h^c\}, \tag{3d}$$

$$M_h^c := \{\mu \in L^2(\mathcal{E}_h^c) \,:\, \mu|_E \in P_0(E), \quad \forall E \in \mathcal{E}_h^c\}, \tag{3e}$$

where $RT_0(S)$ is the Raviart–Thomas space of lowest order on a simplex S, and $P_0(S)$ is the space of constants.

We denote the following inner products:

$$(\phi,\psi)_{\mathcal{T}_h} := \sum_{K\in\mathcal{T}_h}\int_K \phi\,\psi\,\mathrm{dx}, \qquad \langle\phi,\psi\rangle_{\partial\mathcal{T}_h} := \sum_{K\in\mathcal{T}_h}\int_{\partial K} \phi\,\psi\,\mathrm{ds},$$

$$\langle\phi,\psi\rangle_{\mathcal{T}_h^c} := \sum_{F\in\mathcal{T}_h^c}\int_F \phi\,\psi\,\mathrm{ds}, \qquad [\phi,\psi]_{\partial\mathcal{T}_h^c} := \sum_{F\in\mathcal{T}_h^c}\int_{\partial F} \phi\,\psi\,\mathrm{dr},$$

where dx is for d-dimensional integration, ds is for $(d-1)$-dimensional integration, and dr is for $(d-2)$-dimensional integration. When $d=2$, $\int_{\partial F}\phi\,\psi\mathrm{dr}$ is simply the sum of point evaluations at the two end points of a line segment F.

3.2. The hybrid-mixed method for the flow model

The hybrid-mixed method for the hybrid-dimensional model (1) is given as follows: Find $(\boldsymbol{u}_h, p_h, \widehat{p}_h, \boldsymbol{u}_h^c, \widehat{p}_h^c) \in \boldsymbol{V}_h \times W_h \times M_h \times \boldsymbol{V}_h^c \times M_h^c$ with $\widehat{p}_h|_{\Gamma_D} = \mathbb{P}_0(p_D)$ and $\widehat{p}_h^c|_{\Gamma_{cm}^D} = \mathbb{P}_0(p_D)$, where $\mathbb{P}_0$ denotes the projection onto piecewise constants, such that

$$(\mathbb{K}_m^{-1}\boldsymbol{u}_h, \boldsymbol{v}_h)_{\mathcal{T}_h} + \int_{\Omega_b}\frac{\epsilon}{K_b}(\boldsymbol{u}_h\cdot\boldsymbol{n})(\boldsymbol{v}_h\cdot\boldsymbol{n})\mathrm{ds} - (p_h, \nabla\cdot\boldsymbol{v}_h)_{\mathcal{T}_h} + \langle\widehat{p}_h, \boldsymbol{v}_h\cdot\boldsymbol{n}\rangle_{\partial\mathcal{T}_h} = 0, \tag{4a}$$

$$(\nabla\cdot\boldsymbol{u}_h, q_h)_{\mathcal{T}_h} - (f, q_h)_{\mathcal{T}_h} = 0, \tag{4b}$$

$$-\langle\boldsymbol{u}_h\cdot\boldsymbol{n}, \widehat{q}_h\rangle_{\partial\mathcal{T}_h} + \langle\nabla_\Gamma\cdot\boldsymbol{u}_h^c, \widehat{q}_h\rangle_{\mathcal{T}_h^c} + \int_{\Gamma^N} q_N\,\widehat{q}_h\,\mathrm{ds} = 0, \tag{4c}$$

$$\langle(\epsilon\mathbb{K}_c)^{-1}\boldsymbol{u}_h^c, \boldsymbol{v}_h^c\rangle_{\mathcal{T}_h^c} - \langle\widehat{p}_h, \nabla_\Gamma\cdot\boldsymbol{v}_h^c\rangle_{\mathcal{T}_h^c} + [\widehat{p}_h^c, \boldsymbol{v}_h^c\cdot\boldsymbol{\eta}]_{\partial\mathcal{T}_h^c} + \int_{\Gamma_{cb}}\alpha(\epsilon\mathbb{K}_c)^{-1}(\boldsymbol{u}_h^c\cdot\boldsymbol{\eta})(\boldsymbol{v}_h^c\cdot\boldsymbol{\eta})\,\mathrm{dr} = 0, \tag{4d}$$

$$-[\boldsymbol{u}_h^c\cdot\boldsymbol{\eta}, \widehat{q}_h^c]_{\partial\mathcal{T}_h^c} = 0, \tag{4e}$$

for all $(\boldsymbol{v}_h, q_h, \widehat{q}_h, \boldsymbol{v}_h^c, \widehat{q}_h^c) \in \boldsymbol{V}_h \times W_h \times M_h \times \boldsymbol{V}_h^c \times M_h^c$ with $\widehat{q}_h|_{\Gamma_D} = \widehat{q}_h^c|_{\Gamma_{cm}^D} = 0$, where $\alpha > 0$ is a penalty parameter for the implementation of the no-flow boundary condition (1j) on Γ_{cb}. In our numerical implementation, we take $\alpha = 10^6$.

We show that the scheme (4) is formally consistent with the hybrid-dimensional model (1):

1. Eq. (4a) is a discretization of the Darcy's law (1a) in the bulk using integration-by-parts and the following property of Dirac-δ function:
$$\int_{\Omega_m}\delta_{\Omega_b}\phi\mathrm{dx} = \int_{\Omega_b}\phi\,\mathrm{ds}.$$
2. Eq. (4b) is the discretization of mass conservation (1b) in the bulk.
3. Eq. (4c) simultaneously enforces (i) the continuity of normal velocity $\boldsymbol{u}_h\cdot\boldsymbol{n}$ across interior element boundaries $\mathcal{E}_h\backslash(\mathcal{T}_h^c\cup\Gamma_N)$, (ii) the boundary condition (1f) on Γ_N, and (iii) mass conservation (1d) within the conductive fractures in $\mathcal{T}_h^c$.
4. Eq. (4d) is a discretization of the Darcy's law (1c) on the conductive fractures $\mathcal{T}_h^c$, where the pressure continuity condition (1h) is also strongly enforced as $\widehat{p}_h$ both represents the bulk pressure on the element boundary $\mathcal{E}_h$ and the pressure within the conductive fracture $\mathcal{T}_h^c$. Moreover, the last term in (4d) is a penalty formulation of the no-flow boundary condition (1j) on Γ_{cb}. Note that Γ_{cb} is allowed to be not aligned with the facets of $\mathcal{T}_h^c$.
5. Eq. (4e) is a transmission condition that simultaneously enforces (i) continuity of in-plane normal velocity $\boldsymbol{u}_h^c\cdot\boldsymbol{\eta}$ on interior facets $E_h^c\backslash\{\Gamma_{cc}\cup\Gamma_{cm}^N\cup\Gamma_{ci}\}$, (ii) the mass conservation (1h) on the intersections Γ_{cc} (iii) the no-flow boundary condition (1j) on Γ_{cm}^N and Γ_{ci}.
6. The Dirichlet boundary condition (1e) and (1i) are imposed strongly through the corresponding degrees of freedom (DOFs) on $\widehat{p}_h$ and $\widehat{p}_h^c$, respectively.

The following result further shows that the scheme (4) is well-posed.

Theorem 3.1. *Assume the measure of the Dirichlet boundary Γ_D is not empty, then the solution to the scheme (4) exists and is unique.*

Proof. Since the equations in (4) leads to a square linear system, we only need to show uniqueness. Now we assume the source terms in (4) vanishes, i.e., $f = p_D = g_N = 0$. Taking test function to be the same as trial functions in (4) and adding, we get

$$(\mathbb{K}_m^{-1}\boldsymbol{u}_h, \boldsymbol{u}_h)_{\mathcal{T}_h} + \int_{\Omega_b} \frac{\epsilon}{K_b}(\boldsymbol{u}_h \cdot \boldsymbol{n})^2 \, \mathrm{ds} + \langle (\epsilon \mathbb{K}_c)^{-1}\boldsymbol{u}_h^c, \boldsymbol{u}_h^c \rangle_{\mathcal{T}_h^c} = 0.$$

Hence, $\boldsymbol{u}_h = \boldsymbol{u}_h^c = 0$. Since $\boldsymbol{u}_h = 0$, the inf–sup stability of the $RT_0 - P_0$ finite element pair implies that $p_h = \widehat{p}_h = C$ from (4a) where C is a constant. Since Γ_D is not empty and $p_D = 0$, we get the constant $C = 0$. Finally, restricting Eq. (4d) to a single element $F \in \mathcal{T}_h^c$ and using the fact that $\boldsymbol{u}_h^c = 0$ and $\widehat{p}_h = 0$, we get

$$\int_{\partial F} \widehat{p}_h^c \boldsymbol{v}_h^c \cdot \boldsymbol{\eta} \, \mathrm{ds} = 0, \quad \forall \boldsymbol{v}_h^c \in RT_0(F),$$

which then implies that $\widehat{p}_h^c = 0$. This completes the proof. □

3.3. Static condensation and linear system solver

The linear system (4) can be efficiently solved via static condensation, where the DOFs for $\boldsymbol{u}_h$, p_h, and $\boldsymbol{u}_h^c$ can be locally eliminated, resulting in a coupled global linear system for the DOFs for $\widehat{p}_h$ and $\widehat{p}_h^c$, which is symmetric and positive definite. Efficient linear system solvers for the resulting condensed system is an interesting topic where one could design efficient decoupling algorithms or robust monolithic preconditioners. Here we simply use a sparse direct solver in the computation and postpone the detailed study of linear system solvers to our future work.

3.4. Local pressure postprocessing

We use the following well-known local (piecewise linear) pressure postprocessing to improve the accuracy of pressure approximation in the bulk: find

$$p_h^* \in W_h^* := \{w \in L^2(\mathcal{T}_h) : \; w|_K \in P_1(K), \quad \forall K \in \mathcal{T}_h\},$$

where $P^1(K)$ is the space of linear polynomials on element K, such that

$$(\nabla p_h^*, \nabla q_h^*)_{\mathcal{T}_h} = -(\mathbb{K}_m^{-1}\boldsymbol{u}_h, \nabla q_h^*)_{\mathcal{T}_h}, \tag{5a}$$

$$(p_h^*, 1)_{\mathcal{T}_h} = (p_h, 1)_{\mathcal{T}_h}, \tag{5b}$$

for all $q_h^* \in W_h^*$.

3.5. The hybridized finite volume method for the transport model

We consider a standard cell-centered, first-order upwinding finite volume scheme for the transport model (2), coupled with the implicit Euler method for the temporal discretization. We hybridize the cell-centered finite volume scheme so that the coupled unknowns live on the mesh skeletons, which simplifies the definition of upwinding fluxes on the conductive fracture interactions (e.g. point H in Fig. 1). Hence we use piecewise constant spaces to approximate the matrix concentration $c_h \in W_h$ on the mesh $\mathcal{T}_h$, the matrix concentration $\widehat{c}_h \in M_h$ on the matrix mesh skeleton $\mathcal{E}_h$, and the fracture concentration $\widehat{c}_{c,h} \in M_h^c$ on the fracture mesh skeleton $\mathcal{E}_h^c$.

The hybridized finite volume scheme with implicit Euler temporal discretization is given as follows: given data $(c_h^{n-1}, \widehat{c}_h^{n-1}) \in W_h \times M_h$ at time t^{n-1}, find $(c_h^n, \widehat{c}_h^n, \widehat{c}_{c,h}^n) \in W_h \times M_h \times M_h^c$ at time $t^n := t^{n-1} + \Delta t$ with $\widehat{c}_h^n|_{\partial\Omega_{in}} = P_0(c_B(t^n))$ and $\widehat{c}_{c,h}^n|_{\Gamma_{in}} = P_0(c_{c,B}(t^n))$ such that

$$\left(\phi_m \frac{c_h^n - c_h^{n-1}}{\Delta t}, d_h\right)_{\mathcal{T}_h} + \langle \boldsymbol{u}_h \cdot \boldsymbol{n}\widehat{c}_h^{n,*}, d_h\rangle_{\partial\mathcal{T}_h} = \left(c_h^n f, d_h\right)_{\mathcal{T}_h}, \tag{6a}$$

$$-\langle \boldsymbol{u}_h \cdot \boldsymbol{n}\widehat{c}_h^{n,*}, \widehat{d}_h\rangle_{\partial\mathcal{T}_h} + \left\langle \epsilon\phi_c \frac{\widehat{c}_h^n - \widehat{c}_h^{n-1}}{\Delta t}, \widehat{d}_h \right\rangle_{\mathcal{T}_h^c} + [\boldsymbol{u}_h^c \cdot \boldsymbol{\eta}\widehat{c}_{c,h}^{n,*}, \widehat{d}_h]_{\partial\mathcal{T}_h^c} = 0, \tag{6b}$$

$$[\boldsymbol{u}_h^c \cdot \boldsymbol{\eta}\widehat{c}_{c,h}^{n,*}, \widehat{d}_{c,h}]_{\partial\mathcal{T}_h^c} = 0, \tag{6c}$$

for all $(d_h, \widehat{d}_h, \widehat{d}_{c,h}) \in W_h \times M_h \times M_h^c$ with $\widehat{d}_h|_{\partial\Omega_{in}} = 0$ and $\widehat{d}_{c,h}|_{\Gamma_{in}} = 0$, where the upwinding fluxes are given as follows:

$$\widehat{c}_h^{n,*}|_{\partial K} = \begin{cases} c_h^n & \text{if } \boldsymbol{u}_h \cdot \boldsymbol{n}_K > 0, \\ \widehat{c}_h^n & \text{if } \boldsymbol{u}_h \cdot \boldsymbol{n}_K \leq 0, \end{cases} \tag{6d}$$

$$\widehat{c}_{c,h}^{n,*}|_{\partial F} = \begin{cases} \widehat{c}_h^n & \text{if } \boldsymbol{u}_h^c \cdot \boldsymbol{\eta}_F > 0, \\ \widehat{c}_{c,h}^n & \text{if } \boldsymbol{u}_h^c \cdot \boldsymbol{\eta}_F \leq 0. \end{cases} \tag{6e}$$

3.6. Remarks on the mesh restrictions and comparison with existing methods

The proposed flow and transport solvers (4), (6) require the mesh to be fitted to the conductive fractures, while allowing for an unfitted treatment of the blocking fractures. Actually, this is one of the major novelty of the proposed work. While the derivation of numerical schemes that work on fully unfitted meshes is beyond the scope of this paper, here we propose a simple mesh postprocessing technique to convert a general unfitted background matrix mesh to an *immersed* mesh that is fitted to all the fractures. Similar immersing mesh techniques were used for interface problems (Ilinca and Hétu, 2011; Frei and Richter, 2014; Auricchio et al., 2015; Chen et al., 2017). Below we illustrate the procedure of immersing a single fracture to an unfitted tetrahedral mesh in 3D:

(i) Represent the fracture geometry as the zero level set of a continuous piecewise linear function ϕ_h on the background mesh. Perturb ϕ_h slightly if necessary to avoid fracture pass through the background mesh nodes.

(ii) Loop over the background mesh edges, find the cut edges where ϕ_h has opposite sign on the two edge endpoints. For each cut edge, compute the coordinates of the cut vertex v_c where $\phi_h(v_c) = 0$, and add v_c to the mesh nodes.

(iii) Loop over the background mesh faces, find the cut faces which contains the cut vertices. Order the cut vertices based on their vertex label number. Loop over the cut vertices, for each (sub-)face that contains the cut vertex, split the (sub-)face by 2 by connecting the cut vertex with the opposite (sub-)face node.

(iv) Loop over the background mesh elements, find the cut elements which contains the cut vertices. Order the cut vertices based on their vertex label number. Loop over the cut vertices, for each (sub-)element that contains the cut vertex, split the (sub-)element by 2 by connecting the cut vertex with the opposite two (sub-)element nodes that are not aligned with the cut edge.

The above recursive bisection procedure guarantees that the fracture lies on the boundary of the generated immersed mesh. The case with multiply intersecting fractures can be treated by recursion. Here we note that the generated immersed mesh is usually highly anisotropic since the background mesh is completely independent of the fracture configurations. Our numerical results in the next section suggest that the hybrid-mixed method (4) works well on these anisotropic immersed meshes. Typical 2D immersed meshes for complex fracture configurations are given in Figs. 11 and 14.

We now briefly compare our proposed fractured flow solver (4) with some existing schemes in Berre et al. (2021), which were used to solve a series of 4 benchmark problems in 3D fractured porous media flow. Among the 17 schemes in Berre et al. (2021, Table 1), 7 were shown to yield no significant deviations for all the tests, see Berre et al. (2021, Figure 18), which include the multi-point flux approximation (UiB-MPFA), the lowest order mixed virtual element method (UiB-MVEM), and the lowest order Raviart–Thomas mixed finite element method (UiB-RT0) mainly developed by the research group in the University of Bergen (Keilegavlen et al., 2021; Nordbotten et al., 2019; Boon et al., 2018), the MPFA scheme (USTUTT-MPFA) and the two-point flux approximation scheme (USTUTT-TPFA_Circ) developed by Flemisch et al. (2011), the mimetic finite difference method (LANL-MFD) (Lipnikov

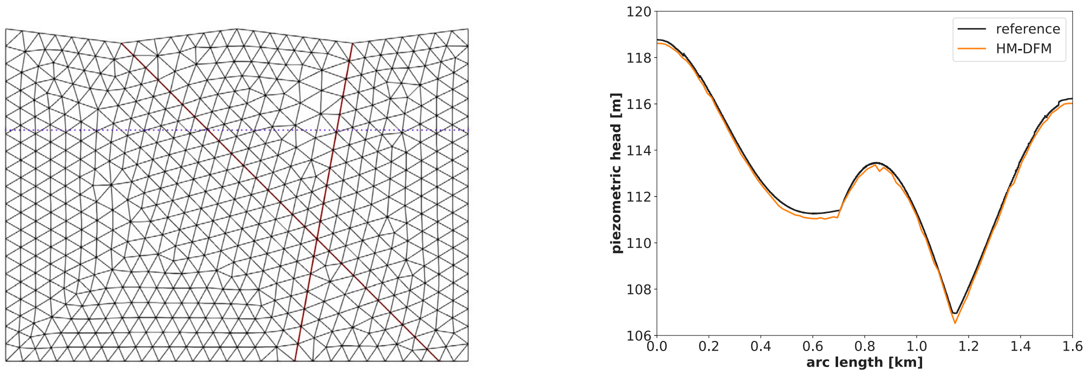

Fig. 3. Benchmark 1. Left: computational mesh. Right: piezometric head along the line $z = -200$ m (dotted blue line on the left figure).

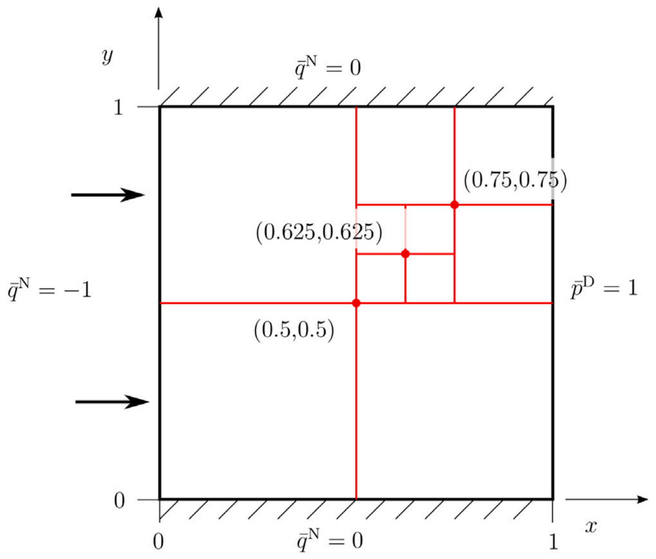

Fig. 4. Benchmark 2. Domain and boundary conditions.

et al., 2014), and the hybrid finite volumes discontinuous hydraulic head method (UNICE_UNIGE-HFV_Disc) developed by Brenner et al. (2017). Among these 7 schemes, the first three schemes use a mixed dimensional interface model that require the modeling of co-dimension 1–3 fractured flows, where the mesh can be non-matching across subdomains, but needs to be geometrically conforming to the fractures. On the other hand, the last four schemes work on a mixed dimensional interface model where only fractured flow in co-dimension 1 were modeled, which require the mesh to be completely conforming to the fractures. All of these schemes yield a locally conservative velocity approximation. We further note that the two methods in Berre et al. (2021) that allow for general nonconforming meshes, namely the Lagrange multiplier method (Köppel et al., 2019a,b; Schädle et al., 2019) and the EDFM method (Nikitin and Yanbarisov, 2020), cannot handle blocking fractures and do not provide a locally conservative velocity approximation.

Numerical results of our proposed scheme (4) for the benchmark problems in Berre et al. (2021) indicate that our results yield no significant deviations with the above mentioned 7 schemes, see details in the next section. Our scheme also produce a locally conservative velocity approximation, and the resulting linear system after static condensation is a symmetric positive definite (SPD) problem with global unknowns involve pressure DOFs on the mesh skeleton only. The number of the global unknowns of our scheme is roughly N_F, which is the total number of mesh faces, and the average nonzero entries per row in the system matrix is 7 (a pressure DOF on an interior tetrahedral face is connected to 6 neighboring face pressure DOFs). Concerning the computational cost of our scheme, it is more expensive than the TPFA scheme (USTUTT-TPFA_Circ) which lead to an SPD system with roughly N_C cell-wise pressure DOFs and about 5 nonzero entries per row in the system matrix, is slightly less expensive than the cell-based MPFA schemes (UiB-MPFA, USTUTT-MPFA), which lead to SPD systems with roughly N_C cell-wise pressure DOFs and about 20–50 nonzero entries per row in the system matrix, and is significantly cheaper than the schemes UiB-MVEM, UiB-RT0, LANL-MFD, and UNICE_UNIGE-HFV_Disc, which lead to saddle point systems with total number of roughly N_F velocity DOFs and N_C pressure DOFs. Note that $N_F \approx 2N_C$. Hence, our proposed scheme is also highly competitive in terms of computational costs. Another distinctive advantage of our scheme over these 7 schemes is that the mesh can be completely nonconforming to the blocking fractures.

4. Numerics

In this section, we present detailed numerical results for the proposed hybrid-mixed method for the four 2D benchmark test cases in Flemisch et al. (2018) and the four 3D benchmark test cases in Berre et al. (2021). We name the method (4) as HM-DFM since it is a hybrid mixed method for a discrete fracture model. When plotting the pressure or hydraulic head distribution over line segments, we evaluate the second-order postprocessed solution in (5) for the proposed method. The focus of the numerical experiments is on the verification of the accuracy of our proposed flow model (1) and the associated method (4). Hence, we test the flow solver (4) for all the 8 benchmark cases. Meanwhile, we also test the accuracy of velocity approximation by feeding them to the transport problem (2), which is solved using the scheme (6) for three cases, namely Benchmark 2 in 2D, and Benchmark 5/6 in 3D. Furthermore, convergence study via mesh refinements was conducted for Benchmark 2 and Benchmark 6 below.

Our numerical simulations are performed using the open-source finite-element software NGSolve (Schöberl, 2014), https://ngsolve.org/. Jupyter notebooks for reproducing all numerical examples in this section can be found in the git repository https://github.com/gridfunction/fracturedPorousMedia. Visualization of meshes for the 3D benchmark examples and interactive contour plots of the pressure/hydraulic head can also be found therein.

4.1. Benchmark 1: Hydrocoin (2D)

This example is originally a benchmark for heterogeneous groundwater flow presented in the international Hydrocoin project (Ski, 1987). A slight modification for the geometry was made in Flemisch et al. (2018, Section 4.1), and we follow the settings therein. In particular, the bulk domain is a polygon with vertices $A = (0, 150)$, $B = (400, 100)$, $C = (800, 150)$, $D = (1200, 100)$, $E = (1600, 150)$, $F = (1600,$

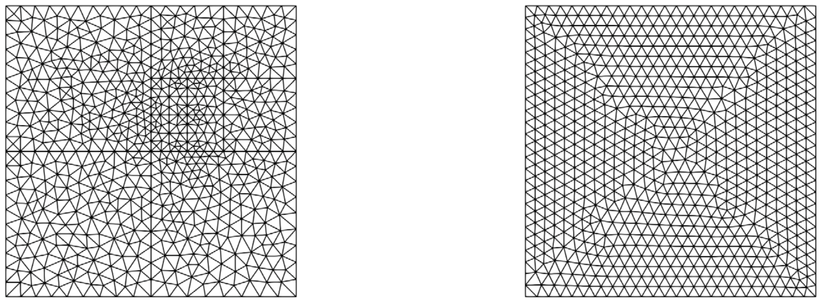

(a) a fitted mesh.

(b) a unfitted mesh.

Fig. 5. Benchmark 2: computational meshes. The fitted mesh on the left panel is used for both conductive and blocking fracture cases. The unfitted mesh on the right panel is used only for the blocking fracture case.

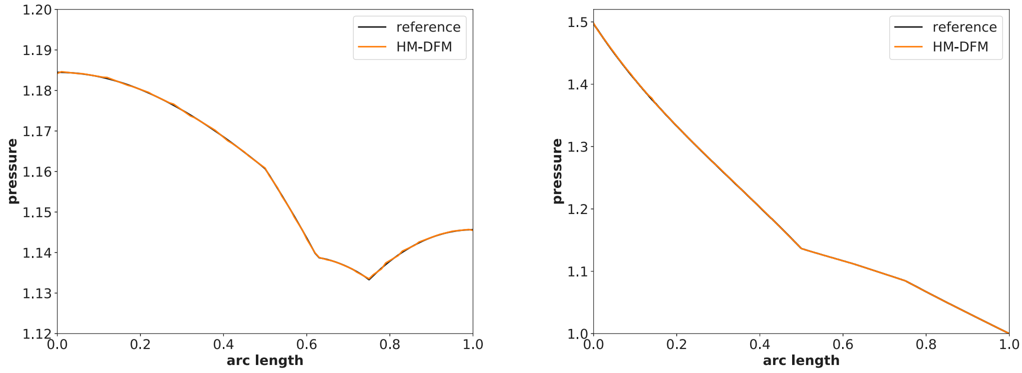

(a) Horizontal line at $y = 0.7$.

(b) Vertical line at $x = 0.5$.

Fig. 6. Benchmark 2 with conductive fractures: pressure distribution along two lines.

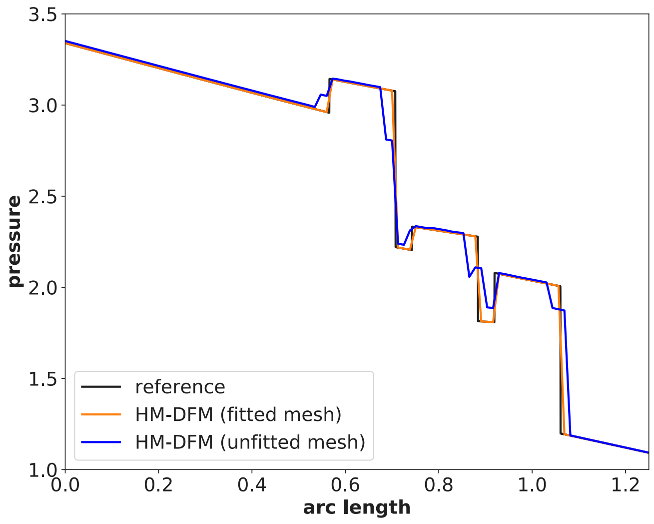

Fig. 7. Benchmark 2 with blocking fractures: values along the line (0,0.1)–(0.9,1.0).

$-1000), G = (1500, -1000), H = (1000, -1000)$ and $I = (0, -1000)$ measured in meters. There are two conductive fractures in the domain $\{BG\}$ and $\{DH\}$. The fracture $\{BG\}$ has thickness $\epsilon = 5\sqrt{2}$ m and the fracture $\{DH\}$ has thickness $\epsilon = 33/\sqrt{5}$ m. The permeability (hydraulic conductivity) is $\mathbb{K}_m = 10^{-8}$ m/s in the bulk and $\mathbb{K}_c = 10^{-6}$ m/s in the fractures. Dirichlet boundary condition $p =$ height is imposed on the top boundary, and homogeneous Neumann boundary condition is imposed on the rest of the boundary. Here the unknown variable p is termed as the piezometric head according to Ski (1987). The quantity of interest is the distribution of the piezometric head p along the horizontal line at a depth of 200 m.

We apply the method (4) on a uniform triangular mesh with mesh size $h = 60$, see the left panel of Fig. 3, which leads to 1115 matrix elements and 44 fracture elements. On this mesh, the number of the globally coupled DOFs is 1779, in which 1691 DOFs are associated with the bulk hybrid variable $\hat{p}_h$, and 43 DOFs are associated with the fracture hybrid variable $\hat{p}_h^c$. In the right panel of Fig. 3, we record the postprocessed piezometric head p_h^* in (5) along the line segment $z = -200$ m, where z is the horizontal direction, along with the reference data obtained from a mimetic finite difference method on a very fine mesh (with 889,233 DOFs). We observe that the results for the proposed method on such a coarse mesh already shows a good agreement with the reference data.

4.2. Benchmark 2: Regular fracture network (2D)

This test case is originally from Geiger et al. (2013) and is modified by Flemisch et al. (2018), which simulates a regular fracture network in a square porous media. The computational domain including the fracture network and boundary conditions is shown in Fig. 4. The matrix permeability is set to $\mathbb{K}_m = \mathbb{I}$, and fracture thickness is $\epsilon = 10^{-4}$. Two cases of fracture permeability was considered: (i) a highly conductive network with $\mathbb{K}_c = 10^4\mathbb{I}$, (ii) a blocking fracture with $K_b = 10^{-4}$.

We apply the method (4) on a triangular mesh with 1348 matrix elements and 91 fracture elements, see the left panel of Fig. 5. For

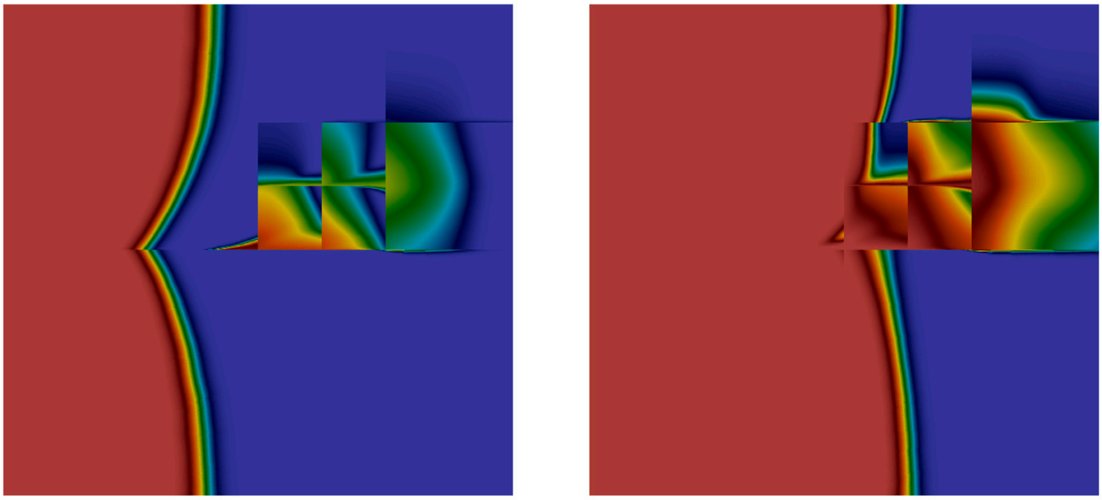

(a) Conductive fractures, $t = 0.05$ (b) Conductive fractures, $t = 0.1$

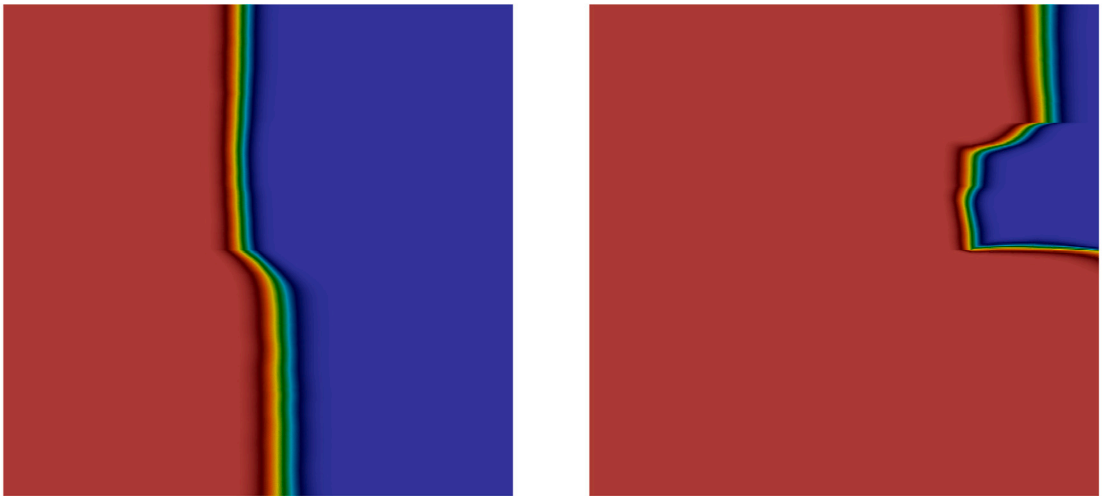

(c) Blocking fractures, $t = 0.05$ (d) Blocking fractures, $t = 0.1$

Fig. 8. Benchmark 2: Matrix concentration at time $t = 0.05$ (left) and $t = 0.1$ (right). Top row: conductive fractures. Bottom row: blocking fractures. Color range: 0(blue)–1(red). Solution obtained on the fourth level refined mesh with a small time step size $\Delta t = 3.125 \times 10^{-5}$. (For interpretation of the references to color in this figure legend, the reader is referred to the web version of this article.)

the blocking fracture case, we also present the result on a unfitted triangular mesh with 1442 matrix elements.

For the conductive fracture case, the number of the globally coupled DOFs is 2127, in which 2041 DOFs are associated with the bulk hybrid variable $\widehat{p}_h$, and 86 DOFs are associated with the fracture hybrid variable $\widehat{p}_h^c$. The pressure distributions along two lines, one horizontal at $y = 0.7$ and one vertical at $x = 0.5$ are shown in Fig. 6, along with the reference data obtained from a mimetic finite difference method on a very fine mesh (with $1,175,056$ DOFs). Similar to the previous example, we observe that the results for the proposed method show a good agreement with the reference data.

For the blocking fracture case, the number of the globally coupled DOFs is 2041 on the fitted mesh and is 2188 on the unfitted mesh. The pressure distribution along the lines $(0, 0.1)$–$(0.9, 1.0)$ is shown in Fig. 7. Again, we observe a very good agreement with reference data for the results on the fitted mesh. The result on the unfitted mesh case is slightly off due to mesh nonconformity, which is expected as it could not capture the pressure discontinuity across the blocking fractures.

4.2.1. Coupling with transport and convergence study with mesh refinements

After the velocity fields are computed from the scheme (4), we feed them to the transport model (2), and solve it by using the hybrid finite volume scheme (6). We take the porosities $\phi_m = 0.1$, $\phi_c = 0.9$ in the model (2), with the initial concentrations $c_0 = c_{c,0} = 0$, and set the left boundary as the inflow boundary for the concentrations, with $c_B = c_{c,B} = 1$. The final time of simulation is $T = 0.1$. Convergence of our coupled scheme (4) and (6) is checked via a mesh refinement study, where the initial meshes are given in Fig. 5, and three level of uniform mesh refinements are applied afterwards. The constant time step size is taken to be $\Delta t = 2^{-l} \times 5 \times 10^{-3}$, where l is the mesh refinement level. Since there is no analytic solution to the problem, we provide a reference solution using the coupled scheme (4) and (6) on the fourth level refined fitted mesh (with about 345k elements) with a small time step size $\Delta t = 3.125 \times 10^{-5}$. Contour of matrix concentrations of the reference solution at time $t = 0.05$ and $t = 0.1$ are presented in Fig. 8, where we clearly observe the conducting and blocking effects of the respective fractures. Moreover, we plot the computed matrix concentrations along the cut line $y = 0.7$ in Fig. 9, where we observe convergence as the mesh refines.

Finally, the L^2-errors in the matrix velocity $\|\boldsymbol{u}_h - \boldsymbol{u}_{ref}\|_{\Omega_m}$, and postprocessed matrix pressure $\|p_h^* - p_{ref}^*\|_{\Omega_m}$, and the L^2-errors in the matrix concentration $\|c_h(T) - c_{ref}(T)\|_{\Omega_m}$ at final time $T = 0.1$ are recorded in Table 1 for the conductive fracture case, in Table 2 for the blocking fracture case on fitted meshes and in Table 3 for the blocking

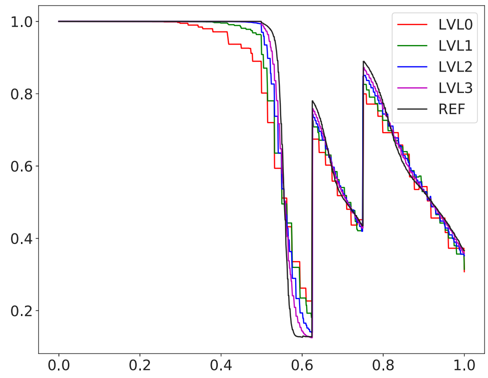

(a) Conductive fractures, fitted mesh

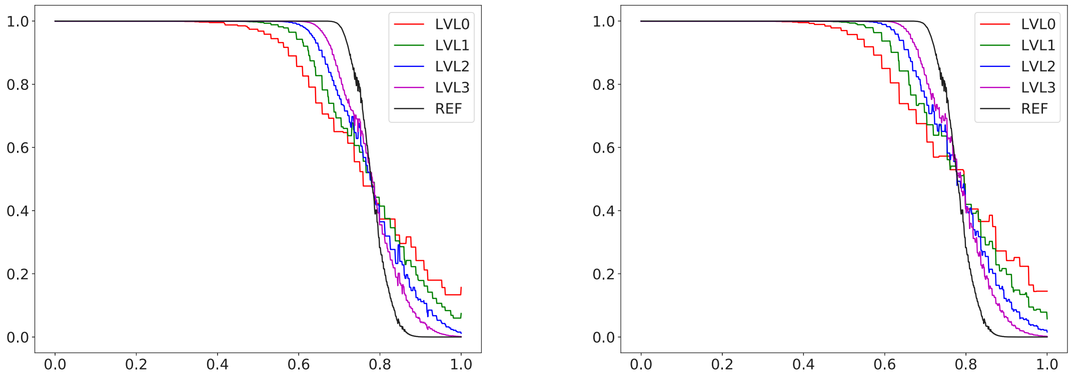

(b) Blocking fractures, fitted mesh

(c) Blocking fractures, unfitted mesh

Fig. 9. Benchmark 2: Matrix concentration along the line $y = 0.7$ at time $t = 0.1$ for the solution on different meshes. LVL stands for the number of mesh refinement levels. Reference solution is obtained on the fourth level refined fitted mesh with a small time step size $\Delta t = 3.125 \times 10^{-5}$.

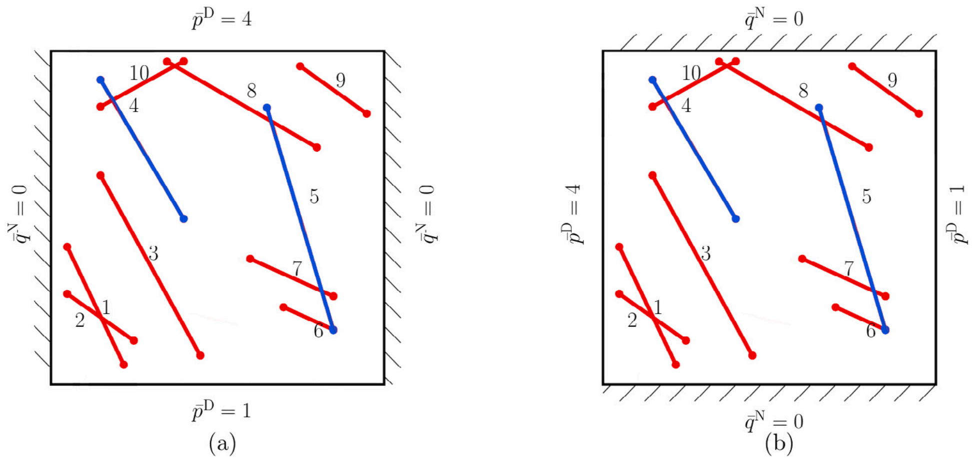

Fig. 10. Benchmark 3: computational domain and boundary conditions.

fracture case on unfitted meshes, where we recall that the reference solutions are obtained on the fourth level refined fitted mesh with a small time step size $\Delta t = 3.125 \times 10^{-5}$. Here the rate of convergence for err at level i is estimated via the formula

$$rate := \log(err_{i-1}/err_i)/\log(2).$$

From Table 1 for the conductive fracture case, we observe that the convergence rate in the velocity approximation is first order and that in the postprocessed pressure approximation is second order, which is consistent with the expected convergence behavior of the hybrid-mixed method for the equi-dimensional case (Raviart and Thomas, 1977; Arnold and Brezzi, 1985), and the convergence rate for the concentration is about 1/2, which is also expected for the hybridized

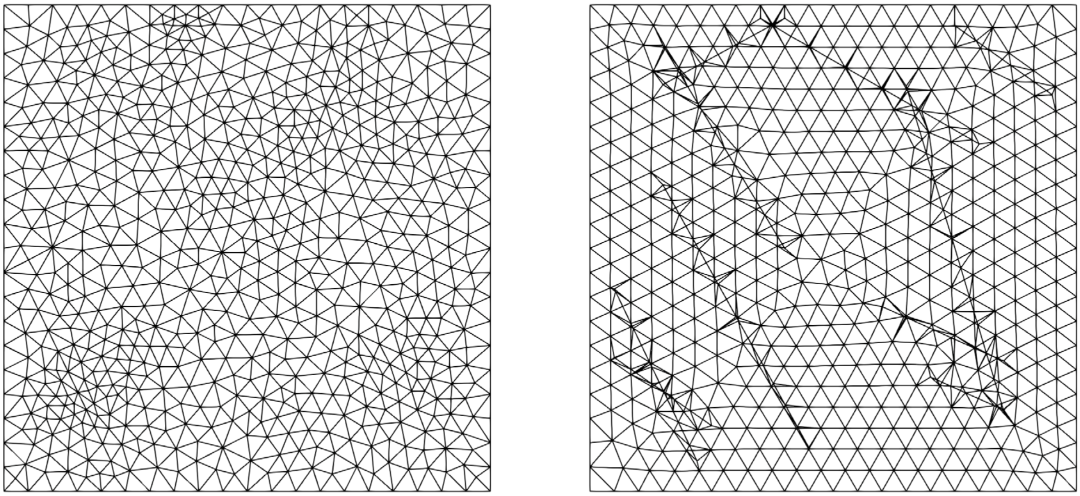

(a) A fitted mesh

(b) An immersed fitted mesh

Fig. 11. Benchmark 3: computational meshes.

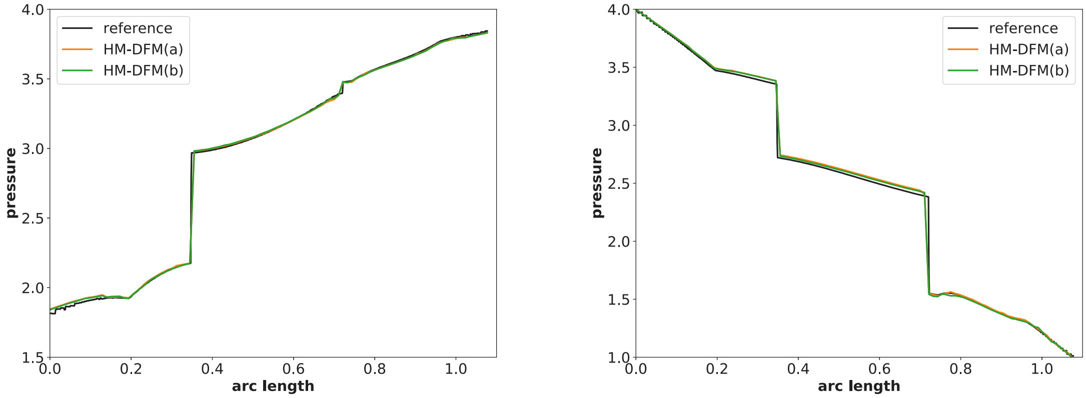

(a) Vertical flow

(b) Horizontal flow

Fig. 12. Benchmark 3: pressure distribution along line $(0, 0.5)$–$(1 - 0.9)$. HDG-DFM(a) is the numerical solution on the fitted mesh in Fig. 11(a), HDG-DFM(b) is the numerical solution on the immersed fitted mesh in Fig. 11(b).

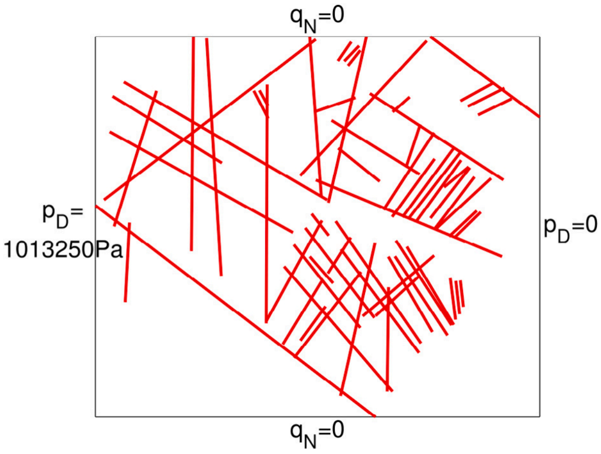

Fig. 13. Benchmark 4: Computational domain and boundary conditions.

Table 1

Benchmark 2 with conductive fractures (fitted mesh): history of convergence for the L^2-errors in $\boldsymbol{u}_h$, p_h^*, and $c_h(T)$ along mesh refinements. Reference solution is obtained on the fourth level refined fitted mesh with a small time step size $\Delta t = 3.125 \times 10^{-5}$.

Mesh ref. lvl.	L^2-err in $\boldsymbol{u}_h$	Rate	L^2-err in p_h^*	Rate	L^2-err in $c_h(T)$	Rate
0	3.567e−02	–	3.786e−04	–	1.177e−01	–
1	1.954e−02	0.87	1.061e−04	1.84	8.587e−02	0.45
2	1.029e−02	0.92	2.863e−05	1.89	5.883e−02	0.55
3	4.881e−03	1.08	7.146e−06	2.00	3.541e−02	0.73

finite volume scheme due to the concentration discontinuities in the domain. Similar convergence behavior was observed in Table 2 for the blocking fracture case on fitted meshes. From Table 3 we observe 1/2 order convergence for all three variables, where the degraded velocity and pressure convergence is due to nonconformity of the mesh with the fractures.

4.3. Benchmark 3: Complex fracture network (2D)

This test case considers a small but complex fracture network that includes permeable and blocking fractures. The domain and boundary

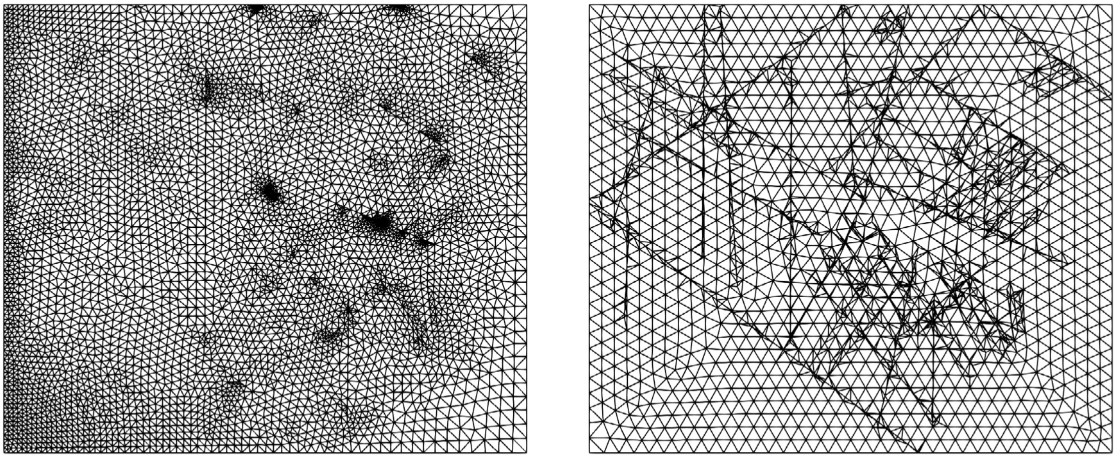

(a) A fitted mesh

(b) An immersed fitted mesh

Fig. 14. Benchmark 4: computational meshes.

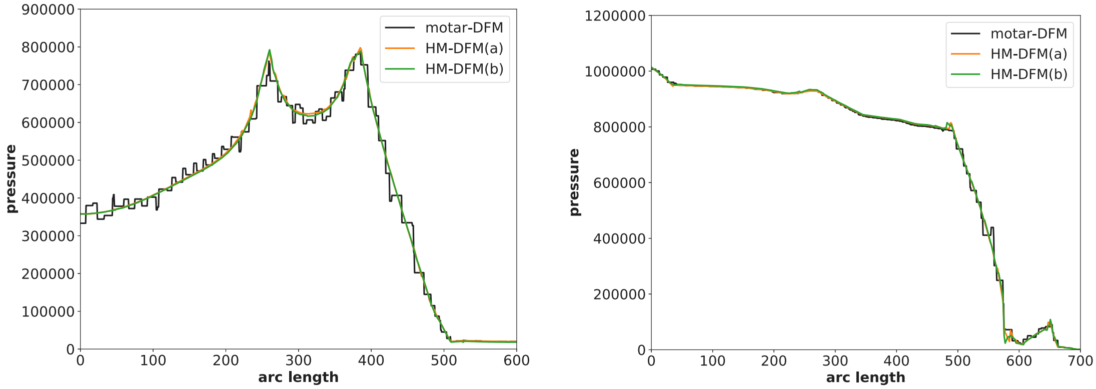

(a) $y = 500m$

(b) $x = 625m$

Fig. 15. Benchmark 4: Pressure distribution along lines $y = 500$ m (left) and $x = 625$ m (right). HDG-DFM(a) is the numerical solution on the fitted mesh in Fig. 14(a), HDG-DFM(b) is the numerical solution on the immersed fitted mesh in Fig. 14(b).

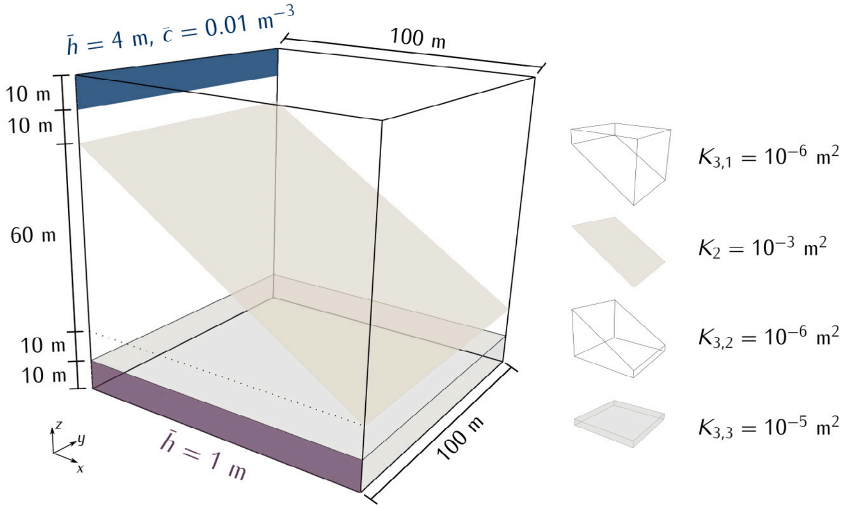

Fig. 16. Benchmark 5: Conceptual model and geometrical description of the domain.

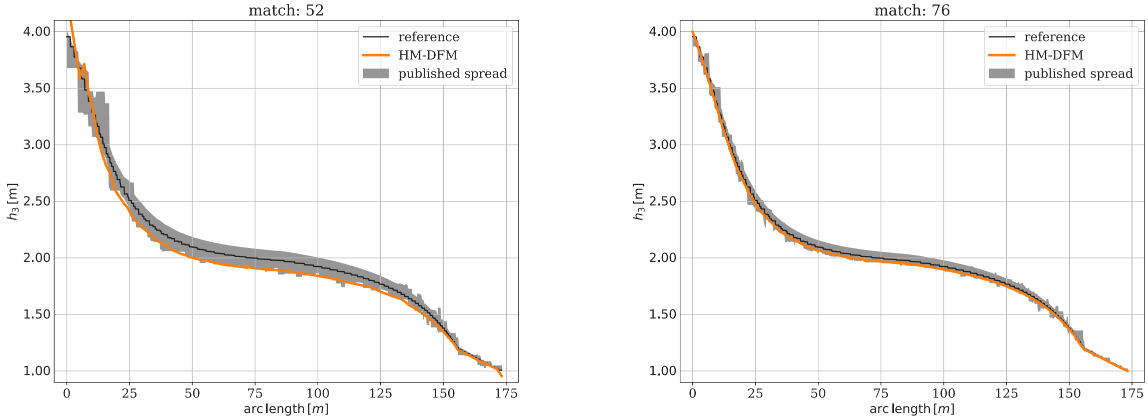

(a) $\sim 10k$ cells.

(b) $\sim 100k$ cells.

Fig. 17. Benchmark 5: Hydraulic head in the matrix over the line (0 m, 100 m, 100 m)–(100 m, 0 m, 0 m). Left: results on a coarse mesh with about 10k cells. Right: results on a fine mesh with about 100k cells.

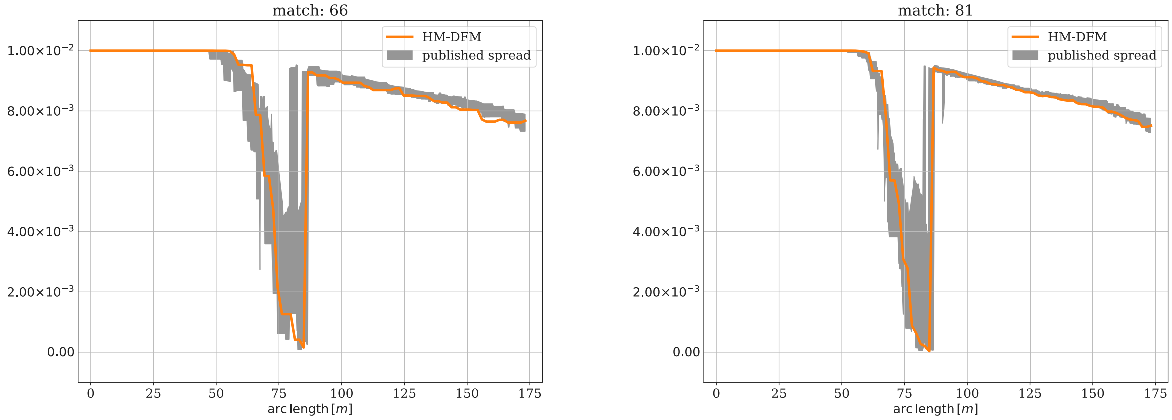

(a) $\sim 10k$ cells.

(b) $\sim 100k$ cells.

Fig. 18. Benchmark 5: Hydraulic head in the matrix over the line (0 m, 100 m, 100 m)–(100 m, 0 m, 0 m). Left: results on a coarse mesh with about 10k cells. Right: results on a fine mesh with about 100k cells.

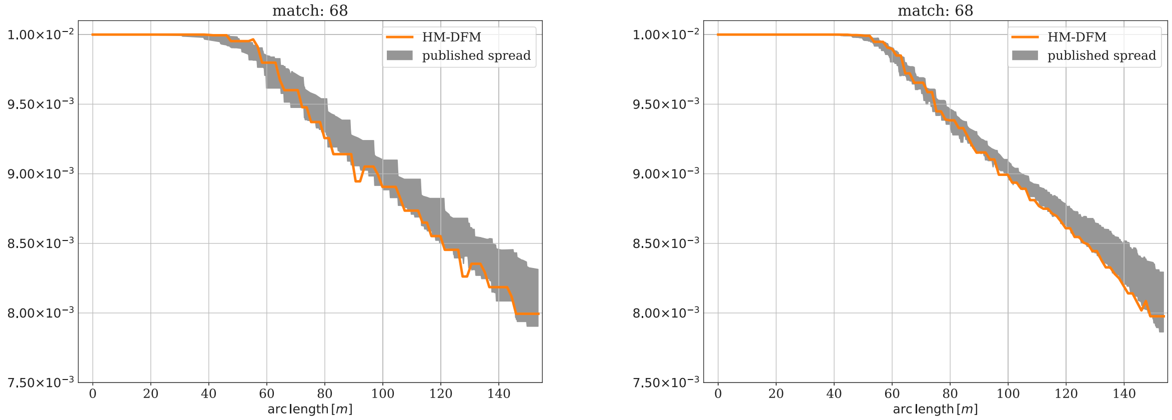

(a) $\sim 10k$ cells.

(b) $\sim 100k$ cells.

Fig. 19. Benchmark 5: Fracture concentration over the line (0 m, 100 m, 80 m)–(100 m, 0 m, 20 m). Left: results on a coarse mesh with about 10k cells. Right: results on a fine mesh with about 100k cells.

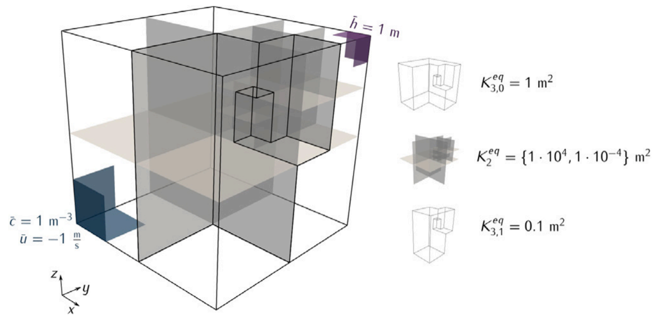

Fig. 20. Benchmark 6: Conceptual model and geometrical description of the domain.

Table 2
Benchmark 2 with blocking fractures (fitted mesh): history of convergence for the L^2-errors in $\boldsymbol{u}_h$, p^*_h, and $c_h(T)$ along mesh refinements. Reference solution is obtained on the fourth level refined fitted mesh with a small time step size $\Delta t = 3.125 \times 10^{-5}$.

Mesh ref. lvl.	L^2-err in $\boldsymbol{u}_h$	Rate	L^2-err in p^*_h	Rate	L^2-err in $c_h(T)$	Rate
0	1.358e−02	–	2.406e−04	–	1.396e−01	–
1	7.098e−03	0.94	6.402e−05	1.91	1.025e−01	0.44
2	3.607e−03	0.98	1.630e−05	1.97	7.149e−02	0.52
3	1.666e−03	1.11	3.566e−06	2.19	4.572e−02	0.64

Table 3
Benchmark 2 with blocking fractures (unfitted mesh): history of convergence for the L^2-errors in $\boldsymbol{u}_h$, p^*_h, and $c_h(T)$ along mesh refinements. Reference solution is obtained on the fourth level refined fitted mesh with a small time step size $\Delta t = 3.125 \times 10^{-5}$.

Mesh ref. lvl.	L^2-err in $\boldsymbol{u}_h$	Rate	L^2-err in p^*_h	Rate	L^2-err in $c_h(T)$	Rate
0	7.611e−02	–	8.295e−02	–	1.424e−01	–
1	5.357e−02	0.51	5.890e−02	0.49	1.050e−01	0.44
2	3.991e−02	0.42	4.088e−02	0.53	7.418e−02	0.50
3	2.634e−02	0.60	2.899e−02	0.50	4.882e−02	0.60

conditions are shown in Fig. 10. The exact coordinates for the fracture positions are provided in Flemisch et al. (2018, Appendix C). The fracture network contains ten straight immersed fractures. The fracture thickness is $\epsilon = 10^{-4}$ for all fractures, and permeability is $\mathbb{K}_c = 10^4$ for all fractures except for fractures 4 and 5 which are blocking fractures with $K_b = 10^{-4}$. Note that we are considering two subcases (a) and (b) with a pressure gradient which is predominantly vertical and horizontal respectively.

We apply the method (4) on two set of meshes: a triangular fitted mesh with 1332 matrix elements and 88 fracture elements which was provided in the git repository https://git.iws.uni-stuttgart.de/benchmarks/fracture-flow, see left of Fig. 11, and a triangular immersed fitted mesh with 1370 matrix elements and 211 fracture elements obtained from a background unfitted mesh using the immersing mesh technique introduced in Section 3.6, see right of Fig. 11. The globally coupled DOFs is 2066 for the fitted mesh, and is 2211 for the immersed mesh. The pressure distributions along the lines $(0, 0.5)$–$(1.0, 0.9)$ are shown in Fig. 12. We observe that the results on the two meshes are very close to each other, and they are in good agreements with the reference data obtained from a mimetic finite difference method on a very fine mesh with 1.8 million DOFs.

4.4. Benchmark 4: a realistic case (2D)

We consider a real set of fractures from an interpreted outcrop in the Sotra island, near Bergen in Norway. The size of the domain is 700 m × 600 m with uniform scalar permeability $\mathbb{K}_m = 10^{-14}$ m^2. The set of fractures is composed of 64 line segments, in which the permeability is $\mathbb{K}_c = 10^{-8}$ m^2. The fracture thickness is $\epsilon = 10^{-2}$ m. The exact coordinates for the fracture positions are provided in the above mentioned git repository. The domain along with boundary conditions is given in Fig. 13. Similar to the previous example, we apply the method (4) on two set of conforming meshes: a fitted mesh consists of 10,807 matrix elements and 1047 fracture elements provided in https://git.iws.uni-stuttgart.de/benchmarks/fracture-flow, see left of Fig. 14, and an immersed fitted mesh consists of 5473 matrix elements and 1541 fracture elements obtained from a background unfitted mesh using the immersing mesh technique introduced in Section 3.6, see right of Fig. 14. The number of the globally coupled DOFs is 17,253 for the fitted mesh (a), and 9753 for the immersed mesh (b).

The pressure distribution along the two lines $y = 500$ m and $x = 625$ m are shown in Fig. 15, along with the results for the mortar-DFM method with 25,258 DOFs from Flemisch et al. (2018). We observe that the three results are in good agreements with each other, with the HDG-DFM(b) using the least amount of DOFs.

4.5. Benchmark 5: Single fracture (3D)

This is the first benchmark case proposed in Berre et al. (2021). To be consistent with the notation in Berre et al. (2021), the pressure and permeabilities are renamed as hydraulic head and hydraulic conductivities, respectively for this test case and the three examples following. Fig. 16 illustrates the geometrical description. Here the domain Ω is a cube-shaped region $(0\text{ m}, 100\text{ m}) \times (0\text{ m}, 100\text{ m}) \times (0\text{ m}, 100\text{ m})$ which is crossed by a conductive planar fracture, Ω_2, with a thickness of $\epsilon = 10^{-2}$ m. The matrix domain consists of subdomains $\Omega_{3,1}$, above the fracture, and $\Omega_{3,2}$ and $\Omega_{3,3}$ below. The subdomain $\Omega_{3,3}$ represents a heterogeneity within the rock matrix. The matrix conductivities are given in Fig. 16, and the fracture conductivity is $\mathbb{K}_c = 0.1$ so that $\epsilon\mathbb{K}_c = 10^{-3}$. Inflow into the system occurs through a narrow band defined by $\{0\text{ m}\} \times (0\text{ m}, 100\text{ m}) \times (90\text{ m}, 100\text{ m})$. Similarly, the outlet is a narrow band defined by $(0\text{ m}, 100\text{ m}) \times \{0\text{ m}\} \times (0\text{ m}, 10\text{ m})$. At the inlet and outlet bands, we impose the hydraulic head $h_{in} = 4$ m and $h_{out} = 1$ m respectively. The remaining parts of the boundary are assigned no-flow conditions. Following the setup in Berre et al. (2021), we set $c_B = 0.01$ m^{-3} at the inlet boundary for the transport problem. The matrix porosity ϕ is taken to be 0.2 on $\Omega_{3,1} \cup \Omega_{3,2}$ and 0.25 on $\Omega_{3,3}$, and the fracture porosity ϕ_c is taken to be 0.4. The final time of simulation is $T = 10^9$ s, and the time step size is $\Delta t = 10^7$ s.

We perform the method (4) and (6) on a coarse tetrahedral mesh with 10,232 matrix elements and 448 fracture elements and a fine tetrahedral mesh with 111,795 matrix elements and 1758 fracture elements. The number of the globally coupled DOFs on the coarse mesh is 23,377, while that on the fine mesh is 235,619. The hydraulic head along the line $(0\text{ m}, 100\text{ m}, 100\text{ m})$–$(100\text{ m}, 0\text{ m}, 0\text{ m})$ is shown in Fig. 17, along with reference data and published spread provided in the git repository https://git.iws.uni-stuttgart.de/benchmarks/fracture-flow-3d. The reference data in Fig. 17 is obtained from the USTUTT-MPFA method on a mesh with approximately 1 million matrix elements, while the shaded region depicts the area between the 10th and the 90th percentile of the published results in Berre et al. (2021) on mesh refinement level 1 (left, $\sim$ 10k cells) and refinement level 2 (right, $\sim$ 100k cells). The match number results from evaluating at 100 evenly distributed evaluation points if the value for the HM-DFM method is between the respective lower and upper value. We observe that our result agrees with the reference values quite well, especially on the fine mesh.

Moreover, we plot the matrix concentration along the line $(0\text{ m}, 100\text{ m}, 100\text{ m})$–$(100\text{ m}, 0\text{ m}, 0\text{ m})$ in Fig. 18, and the fracture concentration along the line $(0\text{ m}, 100\text{ m}, 80\text{ m})$–$(100\text{ m}, 0\text{ m}, 20\text{ m})$ at final time $T = 10^9$ s in Fig. 19, together with the published spread provided in the git repository, which depicts the area between the 10th and the 90th percentile of the published results in Berre et al. (2021) using similar first order finite volume schemes with implicit Euler time stepping and $\Delta t = 10^7$ s. We observe that our results agree quite well with the provided data.

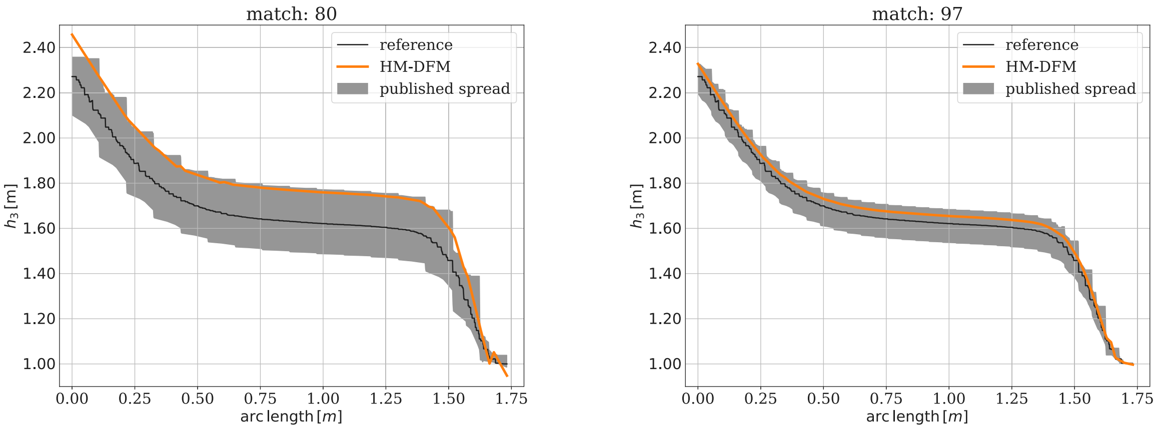

(a) $\sim 4k$ cells.

(b) $\sim 36k$ cells.

Fig. 21. Benchmark 6 (conductive fractures): Hydraulic head in the matrix over the line (0 m, 0 m, 0 m)–(1 m, 1 m, 1 m). Left: results on a coarse mesh with about 4k cells. Right: results on a fine mesh with about 36k cells.

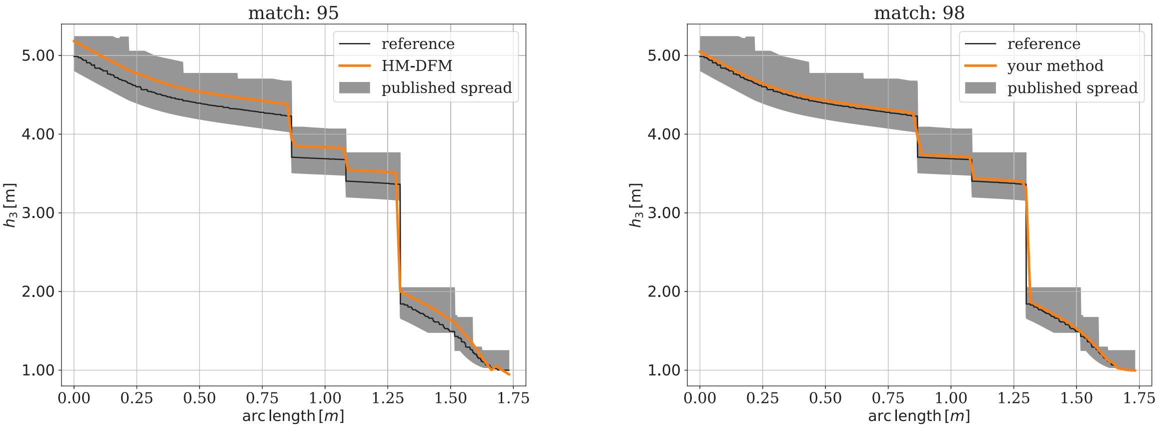

(a) $\sim 4k$ cells.

(b) $\sim 36k$ cells.

Fig. 22. Benchmark 6 (blocking fractures): Hydraulic head in the matrix over the line (0 m, 0 m, 0 m)–(1 m, 1 m, 1 m). Left: results on a coarse mesh with about 4k cells. Right: results on a fine mesh with about 36k cells.

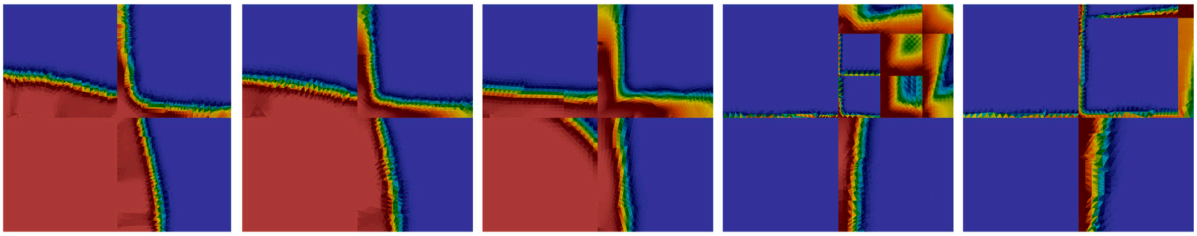

(a) C. c_h on $x = 0.1$ (b) C. c_h on $x = 0.3$ (c) C. c_h on $x = 0.5$ (d) C. c_h on $x = 0.7$ (e) C. c_h on $x = 0.9$

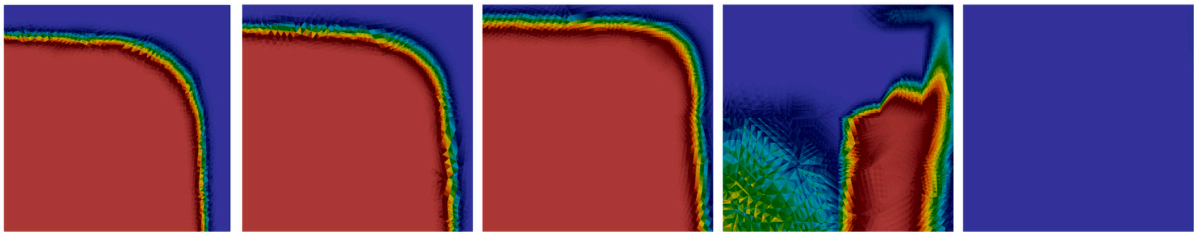

(f) B. c_h on $x = 0.1$ (g) B. c_h on $x = 0.3$ (h) B. c_h on $x = 0.5$ (i) B. c_h on $x = 0.7$ (j) B. c_h on $x = 0.9$

Fig. 23. Benchmark 6: Matrix concentration at time $t = 0.25$ along the five vertical planes $x = 0.1$, $x = 0.3$, $x = 0.5$, $x = 0.7$ and $x = 0.9$. Top row: conductive fractures. Bottom row: blocking fractures. Color range: 0 (blue)– 1(red). (For interpretation of the references to color in this figure legend, the reader is referred to the web version of this article.)

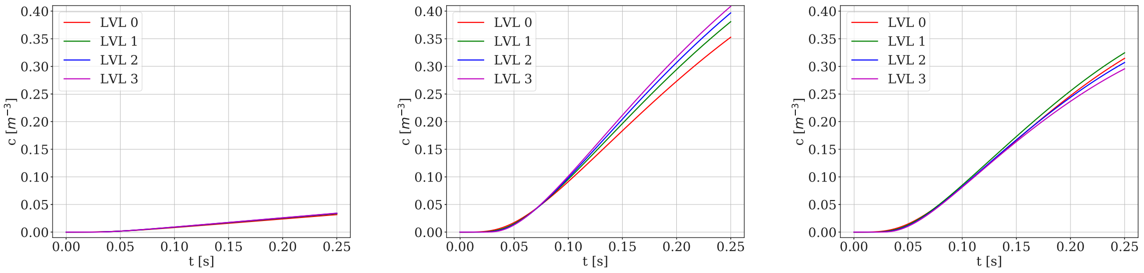

(a) Conductive, mean c_h on Ω_A (b) Conductive, mean c_h on Ω_B (c) Conductive, mean c_h on Ω_C

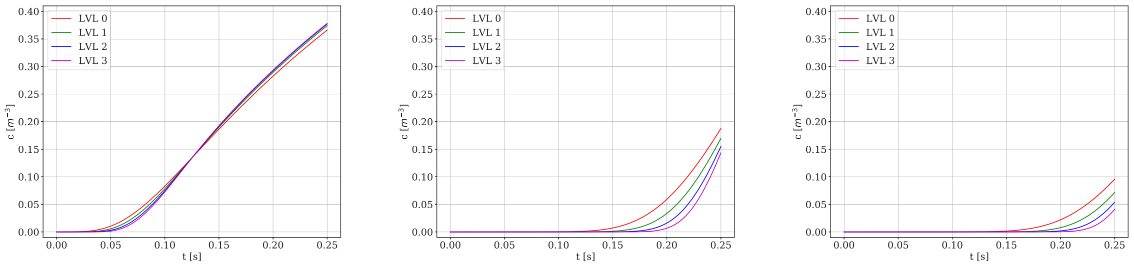

(d) Blocking, mean c_h on Ω_A (e) Blocking, mean c_h on Ω_B (f) Blocking, mean c_h on Ω_C

Fig. 24. Benchmark 6: Mean matrix concentration over time on Ω_A (left), Ω_B (middle), and Ω_C (right). Top row: conductive fractures. Bottom row: blocking fractures. LVL stands for the number of mesh refinement levels.

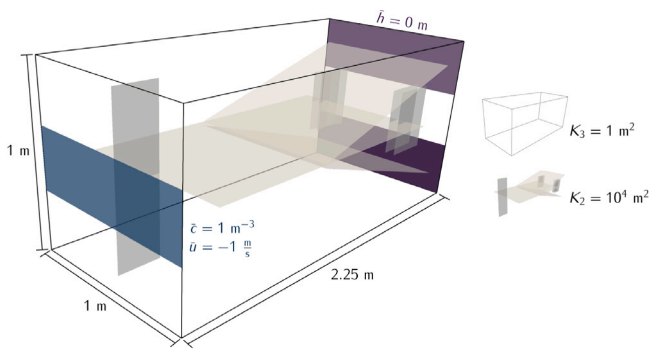

Fig. 25. Benchmark 7: Conceptual model and geometrical description of the domain.

Table 4
Benchmark 6 with conductive fractures (fitted mesh): history of convergence for the L^2-errors in $\boldsymbol{u}_h$, p_h^*, and $c_h(T)$ along mesh refinements. Reference solution is obtained on the third level refined fitted mesh with about 2.25 million matrix elements and time step size $\Delta t = 3.125 \times 10^{-4}$.

Mesh ref. lvl.	L^2-err in $\boldsymbol{u}_h$	Rate	L^2-err in p_h^*	Rate	L^2-err in $c_h(T)$	Rate
0	1.789e−01	–	1.456e−01	–	1.496e−01	–
1	1.120e−01	0.68	5.886e−02	1.31	9.645e−02	0.63
2	6.181e−02	0.86	1.852e−02	1.67	5.102e−02	0.92

4.6. Benchmark 6: Regular fracture network (3D)

This is the second benchmark case proposed in Berre et al. (2021), which is a 3D analog of Benchmark 2. The domain is given by the unit cube $\Omega = (0\text{ m}, 1\text{ m})^3$ and contains 9 regularly oriented fractures, as illustrated in Fig. 20. Dirichlet boundary condition $p = \bar{h} = 1$ m is imposed on the boundary $\Gamma_D = \{(x,y,z) \in \partial\Omega : x,y,z > 0.875\text{ m}\}$, Neumann boundary condition $\boldsymbol{u}\cdot\boldsymbol{n} = -1$ m/s is imposed on the boundary $\partial\Omega_{in} = \{(x,y,z) \in \partial\Omega : x,y,z < 0.25\text{ m}\}$, and no-flow boundary condition is imposed on the remaining boundaries. The heterogeneous matrix conductivity is illustrated in Fig. 20, and the fracture conductivity is either $\mathbb{K}_c = 10^4$ m^2, which represents a conductive fracture or $K_b = 10^{-4}$ m^2 which represents a blocking fracture. The fracture thickness is $\epsilon = 10^{-4}$ m. For the transport equation, matrix porosity is taken to be $\phi = 0.1$, conductive fracture concentration is $\phi_c = 0.9$, and the inflow boundary condition $c_B = 1$ m^{-3} is set on the inlet boundary $\partial\Omega_{in}$. Final time of the simulation is $T = 0.25$ s.

We perform the method (4) on a coarse *fitted* tetrahedral mesh with 4375 matrix elements and 944 fracture elements and a fine tetrahedral mesh with 36,336 matrix elements and 4524 fracture elements. The number of the globally coupled DOFs on the coarse mesh is 13,373 for the conductive fracture case and 8334 for the blocking fracture case (only DOFs for $\widehat{p}_h$ are global DOFs in this case), while that on the fine mesh is 94,738 for the conductive fracture case and 70,881 for the blocking fracture case. The hydraulic head along the diagonal line $(0\text{ m}, 0\text{ m}, 0\text{ m})$–$(1\text{ m}, 1\text{ m}, 1\text{ m})$ is shown in Fig. 21 for the conductive fracture case and in Fig. 22 for the blocking fracture case. We observe that our results agree with the reference values very well, which were obtained from the USTUTT-MPFA method on a mesh with approximately 1 million matrix elements. The small derivation of our result on the left panel of Fig. 21 with the reference data is acceptable due to the use of a very coarse mesh.

We further performed a convergence study of the flow and transport solvers (4) and (6) via mesh refinements, and record the L^2-errors in matrix velocity and postprocessed pressure, and the L^2-errors in matrix concentration at final time $t = 0.25$ in Table 4 for the conductive fracture case and in Table 5 for the blocking fracture case, where the initial mesh is the coarse one with 4375 tetrahedral elements. A total of three uniform mesh refinements was performed, and the solution on the third level mesh was used as the reference solution to calculate the associated errors. The time step size is taken to be $\Delta t = 2^{-l} \times 2.5 \times 10^{-3}$ s, where l is the mesh refinement level. On the finest mesh, there are about 2.25 million tetrahedral elements and 4.5 million globally coupled DOFs. From both tables, we observe convergence of our schemes, and in particular the convergence rate for the velocity is approaching first order, that for the postprocessed pressure is approaching second order, and for the concentration is about first order.

Finally, in Fig. 23 we plot slices of concentrations computed on the 3rd refined mesh at final time $t = 0.25$ along the five vertical planes

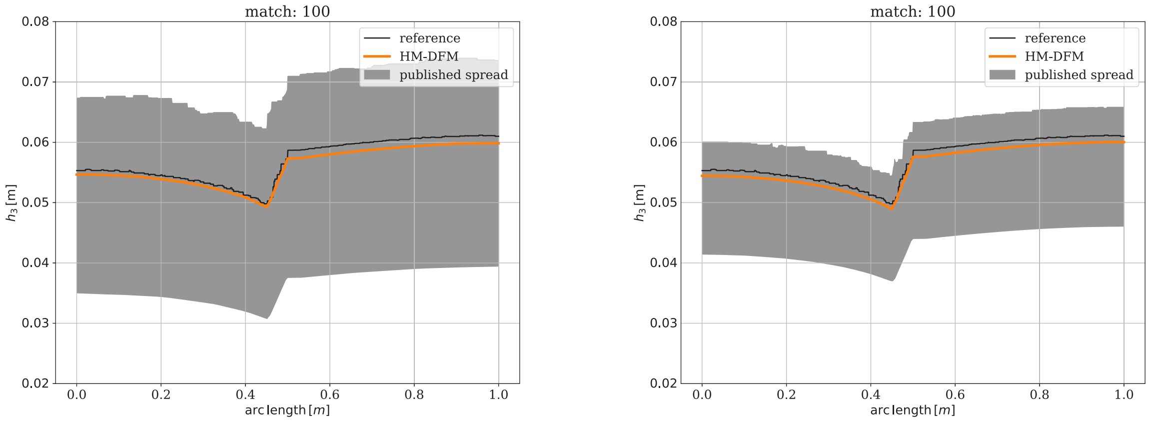

(a) $\sim 32k$ cells.

(b) $\sim 148k$ cells.

Fig. 26. Benchmark 7: Hydraulic head in the matrix over the line (0.5 m, 1.1 m, 0 m)–(0.5 m, 1.1 m, 1 m). Left: results on a coarse mesh with about 32k cells. Right: results on a fine mesh with about 148k cells.

Table 5
Benchmark 6 with blocking fractures (fitted mesh): history of convergence for the L^2-errors in $\boldsymbol{u}_h$, p_h^*, and $c_h(T)$ along mesh refinements. Reference solution is obtained on the third level refined fitted mesh with about 2.25 million matrix elements and time step size $\Delta t = 3.125 \times 10^{-4}$.

Mesh ref. lvl.	L^2-err in $\boldsymbol{u}_h$	Rate	L^2-err in p_h^*	Rate	L^2-err in $c_h(T)$	Rate
0	1.791e−01	–	1.533e−01	–	1.288e−01	–
1	1.118e−01	0.68	6.080e−02	1.33	8.139e−02	0.66
2	6.172e−02	0.86	1.891e−02	1.68	3.939e−02	1.05

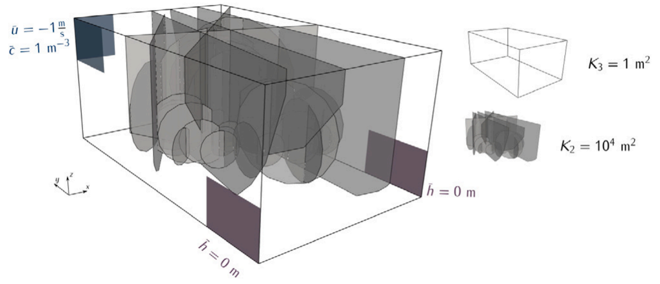

Fig. 27. Benchmark 8: Conceptual model and geometrical description of the domain.

$x = 0.1, x = 0.3, x = 0.5, x = 0.7$ and $x = 0.9$, and in Fig. 24 we plot the evolution of mean concentration over time on the following three regions:

$$\Omega_A := (0.5 \text{ m}, 1 \text{ m}) \times (0 \text{ m}, 0.5 \text{ m}) \times (0 \text{ m}, 0.5 \text{ m}),$$
$$\Omega_B := (0.5 \text{ m}, 0.75 \text{ m}) \times (0.5 \text{ m}, 0.75 \text{ m}) \times (0.75 \text{ m}, 1 \text{ m}),$$
$$\Omega_C := (0.75 \text{ m}, 1 \text{ m}) \times (0.75 \text{ m}, 1 \text{ m}) \times (0.5 \text{ m}, 0.75 \text{ m}).$$

$$\Omega_A := (0.5 \text{ m}, 1 \text{ m}) \times (0 \text{ m}, 0.5 \text{ m}) \times (0 \text{ m}, 0.5 \text{ m}),$$
$$\Omega_B := (0.5 \text{ m}, 0.75 \text{ m}) \times (0.5 \text{ m}, 0.75 \text{ m}) \times (0.75 \text{ m}, 1 \text{ m}),$$
$$\Omega_C := (0.75 \text{ m}, 1 \text{ m}) \times (0.75 \text{ m}, 1 \text{ m}) \times (0.5 \text{ m}, 0.75 \text{ m}).$$

From the results in Fig. 23, we clearly observe the different flow pattern for the conductive fracture case in the first row and the blocking fracture case in the second row. We further note that the mean concentrations reported in Fig. 24 were presented in Berre et al. (2021, Figure 10) (only) on the coarse mesh with about 4k matrix elements and a coarse time step size $\Delta t = 2.5 \times 10^{-3}$ s. Our results on four set of meshes are close to each other and improve slightly as the mesh and time step size refines, and they are also qualitatively similar to the majority of the coarse-grid results in Berre et al. (2021, Figure 10).

4.7. Benchmark 7: Network with small features (3D)

This is the third benchmark case proposed in Berre et al. (2021), in which small geometric features exist that may cause trouble for conforming meshing strategies. The domain is the box $\Omega = (0 \text{ m}, 1 \text{ m}) \times (0 \text{ m}, 2.25 \text{ m}) \times (0 \text{ m}, 1 \text{ m})$, containing 8 fractures; see Fig. 25. Homogeneous Dirichlet boundary condition is imposed on the outlet boundary

$$\partial\Omega_{out} := \{(x, y, z) : 0 < x < 1, y = 2.25, z < 1/3 or z > 2/3\},$$

inflow boundary condition $\boldsymbol{u} \cdot \boldsymbol{n} = -1$ m/s is imposed on the inlet boundary

$$\partial\Omega_{in} := \{(x, y, z) : 0 < x < 1, y = 0, 1/3 < z < 2/3\},$$

and no-flow boundary condition is imposed on the remaining boundaries. The conductivity in the matrix is $\mathbb{K}_m = 1 \text{ m}^2$, and that in the fracture is $\mathbb{K}_c = 10^4 \text{ m}^2$. Fracture thickness is $\epsilon = 0.01$ m.

We perform the method (4) on a coarse tetrahedral mesh with 31,812 matrix elements and 3961 fracture elements and a fine tetrahedral mesh with 147,702 matrix elements and 9441 fracture elements. The number of the globally coupled DOFs on the coarse mesh is 83,022, while that on the fine mesh is 343,359. The hydraulic head along the line (0.5 m, 1.1 m, 0 m)–(0.5 m, 1.1 m, 1 m) is shown in Fig. 26, where the reference data is obtained with the USTUTT-MPFA scheme on a grid with approximately 10^6 matrix cells. Here we observe a very good agreement with the reference data even on the coarse mesh.

4.8. Benchmark 8: Field case (3D)

This is the last benchmark case proposed in Berre et al. (2021). The geometry is based on a postprocessed outcrop from the island of Algerøyna, outside Bergen, Norway, which contains 52 fracture. The simulation domain is the box $\Omega = (-500 \text{ m}, 350 \text{ m}) \times (100 \text{ m}, 1500 \text{ m}) \times (-100 \text{ m}, 500 \text{ m})$. The fracture geometry is depicted in Fig. 27. Homogeneous Dirichlet boundary condition is imposed on the outlet boundary

$$\partial\Omega_{out} := \underbrace{\{-500\} \times (100, 400) \times (-100, 100)}_{\partial\Omega_{out,0}} \cup \underbrace{\{350\} \times (100, 400) \times (-100, 100)}_{\partial\Omega_{out,1}}$$

uniform unit inflow $\boldsymbol{u} \cdot \boldsymbol{n} = 1$ m/s is imposed on the inlet boundary

$$\partial\Omega_{in} := \underbrace{\{-500\} \times (1200, 1500) \times (300, 500)}_{\partial\Omega_{in,0}}$$

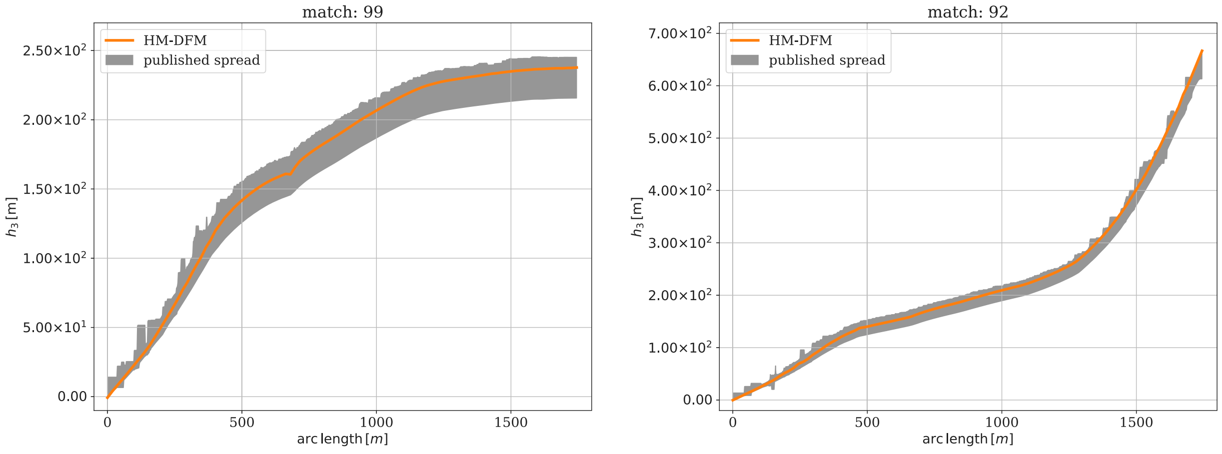

(a) (b)

Fig. 28. Benchmark 8: Hydraulic head across the domain. (a): Profile from outlet $\partial\Omega_{out,0}$ towards the opposite corner. (b): Profile from outlet $\partial\Omega_{out,1}$ towards the opposite corner $\partial\Omega_{in}$.

$$\cup \underbrace{(-500,-200)\times\{1500\}\times(300,500)}_{\partial\Omega_{in,1}}.$$

Conductivity is $\mathbb{K}_m = 1\ \mathrm{m}^2$ in the matrix, and $\mathbb{K}_c = 10^4\ \mathrm{m}^2$ in the fracture. Fracture thickness is $\epsilon = 10^{-2}$ m.

We perform the method (4) on a tetrahedral mesh with 241,338 matrix elements and 47,154 fracture elements. The number of the globally coupled DOFs is 696,487.

The hydraulic head along the two diagonal lines $(-500\ \mathrm{m}, 100\ \mathrm{m}, -100\ \mathrm{m})$–$(350\ \mathrm{m}, 1500\ \mathrm{m}, 500\ \mathrm{m})$ and $(350\ \mathrm{m}, 100\ \mathrm{m}, -100\ \mathrm{m})$–$(-500\ \mathrm{m}, 1500\ \mathrm{m}, 500\ \mathrm{m})$ are shown in Fig. 28, along with published results from Berre et al. (2021). Similar to Benchmark 4 in 2D, no reference data on refined meshes was provided for this problem due to its complexity. Comparing with the published results in Fig. 28 we observe that our method still performs quite well.

5. Conclusion

A novel hybrid-mixed method for single-phase flow in fractured porous media has been presented. The proposed model combines the interface model for the conductive fractures and time Dirac δ-functions approach for the blocking fractures. The distinctive features for the numerical methods include local mass conservation, symmetric positive definite linear system, and allowing the computational mesh to be completely non-conforming to the blocking fractures. Ample benchmark tests show the excellent performance of the proposed scheme, which is also highly competitive with existing work in the literature. Extension to the method to more complex fractured flow models and adaptation of the method to more general meshes consists of our on-going work. We will also investigate efficient preconditioning procedures for the associated linear system problem in the near future.

CRediT authorship contribution statement

Guosheng Fu: Methodology, Software, Writing – original draft, Funding acquisition. **Yang Yang:** Conceptualization, Writing – review & editing, Funding acquisition.

Declaration of competing interest

The authors declare that they have no known competing financial interests or personal relationships that could have appeared to influence the work reported in this paper.

References

Ahmed, R., Edwards, M.G., Lamine, S., Huisman, B.A., Pal, M., 2015. Control-volume distributed multi-point flux approximation coupled with a lower-dimensional fracture model. J. Comput. Phys. 284, 462–489.

Alboin, C., Jaffré, J., Roberts, J., Serres, C., 1999. Domain decomposition for flow in porous media with fractures. In: Lai, M.C.C.H., Bjorstad, P.E., Widlund, O. (Eds.), Domain Decomposition Methods in Sciences and Engineering, Vol. 53. Domain Decomposition Press, Bergen, Norway, pp. 365–373.

Alboin, C., Jaffré, J., Roberts, J., Serres, C., 2002. Modeling fractures as interfaces for flow and transport in porous media. In: Fluid Flow and Transport in Porous Media: Mathematical and Numerical Treatment (South Hadley, MA, 2001). In: Contemp. Math., vol. 295, Amer. Math. Soc., Providence, RI, pp. 13–24.

Alboin, C., Jaffré, J., Roberts, J.E., Wang, X., Serres, C., 2000. Domain decomposition for some transmission problems in flow in porous media. In: Numerical Treatment of Multiphase Flows in Porous Media. Springer, Heidelberg, Berlin, pp. 22–34.

Angot, P., Boyer, F., Hubert, F., 2009. Asymptotic and numerical modelling of flows in fractured porous media. ESAIM Math. Model. Numer. Anal. 43 (2), 239–275.

Antonietti, P.F., Facciola, C., Russo, A., Verani, M., 2019. Discontinuous Galerkin approximation of flows in fractured porous media on polytopic grids. SIAM J. Sci. Comput. 41 (1), A109–A138.

Arnold, D.N., Brezzi, F., 1985. Mixed and nonconforming finite element methods: implementation, postprocessing and error estimates. RAIRO Modél. Math. Anal. Numér. 19 (1), 7–32.

Auricchio, F., Brezzi, F., Lefieux, A., Reali, A., 2015. An "immersed" finite element method based on a locally anisotropic remeshing for the incompressible stokes problem. Comput. Methods Appl. Mech. Engrg. 294, 428–448.

Baca, R.G., Arnett, R.C., Langford, D.W., 1984. Modelling fluid flow in fractured-porous rock masses by finite-element techniques. Internat. J. Numer. Methods Fluids 4 (4), 337–348.

Barenblatt, G.I., Zheltov, I.P., Kochina, I.N., 1960. Basic concepts in the theory of seepage of homogeneous liquids in fissured rocks [strata]. J. Appl. Math. Mech. 24 (5), 1286–1303.

Berre, I., Boon, W., Flemisch, B., Fumagalli, A., Gläser, D., Keilegavlen, E., Scotti, A., Stefansson, I., Tatomir, A., Brenner, K., Burbulla, S., Devloo, P., Duran, O., Favino, M., Hennicker, J., Lee, I.-H., Lipnikov, K., Masson, R., Mosthaf, K., Nestola, M.C., Ni, C.-F., Nikitin, K., Schädle, P., Svyatskiy, D., Yanbarisov, R., Zulian, P., 2021. Verification benchmarks for single-phase flow in three-dimensional fractured porous media. Adv. Water Resour. 147, 103759.

Boon, W., Nordbotten, J., Yotov, I., 2018. Robust discretization of flow in fractured porous media. SIAM J. Numer. Anal. 56, 2203–2233.

Brenner, K., Hennicker, J., Masson, R., Samier, P., 2017. Gradient discretization of hybrid-dimensional Darcy flow in fractured porous media with discontinuous pressures at matrix-fracture interfaces. IMA J. Numer. Anal. 37 (3), 1551–1585.

Burman, E., Hansbo, P., Larson, M.G., Larsson, K., 2019. Cut finite elements for convection in fractured domains. Comput. & Fluids 179, 726–734.

Chen, L., Wei, H., Wen, M., 2017. An interface-fitted mesh generator and virtual element methods for elliptic interface problems. J. Comput. Phys. 334, 327–348.

Fang, W., Liu, C., Li, J., Jiang, H., Pu, J., Gu, H., Qin, X., 2018. A discrete modeling framework for reservoirs with complex fractured media: Theory, validation and case studies. J. Pet. Sci. Eng. 170, 945–957.

Feng, W., Guo, H., Xu, Z., Yang, Y., 2021. Conservative numerical methods for the reinterpreted discrete fracture model on non-conforming meshes and their applications in contaminant transportation in fractured porous media. Adv. Water Resour. 153, 103951.

Flemisch, B., Berre, I., Boon, W., Fumagalli, A., Schwenck, N., Scotti, A., Stefansson, I., Tatomir, A., 2018. Benchmarks for single-phase flow in fractured porous media. Adv. Water Resour. 111, 239–258.

Flemisch, B., Darcis, M., Erbertseder, K., Faigle, B., Lauser, A., Mosthaf, K., Müthing, S., Nuske, P., Tatomir, A., Wolff, M., Helmig, R., 2011. Dumux: DUNE for multi-phase,component,scale, physics,… flow and transport in porous media. Adv. Water Resour. 34 (9), 1102–1112, New Computational Methods and Software Tools.

Flemisch, B., Fumagalli, A., Scotti, A., 2016. A review of the XFEM-based approximation of flow in fractured porous media. In: Advances in Discretization Methods. Springer, Cham, pp. 47–76.

Frei, S., Richter, T., 2014. A locally modified parametric finite element method for interface problems. SIAM J. Numer. Anal. 52 (5), 2315–2334.

Fumagalli, A., Scotti, A., 2013. A reduced model for flow and transport in fractured porous media with non-matching grids. In: Numerical Mathematics and Advanced Applications 2011. Springer, Heidelberg, pp. 499–507.

Fumagalli, A., Scotti, A., 2014. An efficient XFEM approximation of Darcy flows in arbitrarily fractured porous media. Oil Gas Sci. Technol.–Rev. D'IFP Energies Nouv. 69 (4), 555–564.

Geiger, S., Dentz, M., Neuweiler, A.I., 2013. Novel multi-rate dual-porosity model for improved simulation of fractured and multiporosity reservoirs. SPE J. 0 4, 670–684.

Geiger-Boschung, S., Matth"ai, S.K., Niessner, J., Helmig, R., 2009. Black-oil simulations for three-component, three-phase flow in fractured porous media. SPE J. 14 (02), 338–354.

Ghorayeb, K., Firoozabadi, A., 2000. Numerical study of natural convection and diffusion in fractured porous media. Spe J. 5, 12–20.

Gl"aser, D., Helmig, R., Flemisch, B., Class, H., 2017. A discrete fracture model for two-phase flow in fractured porous media. Adv. Water Resour. 110, 335–348.

Golian, M., Katibeh, H., Singh, V.P., Ostad-Ali-Askari, K., Rostami, H., 2020. Prediction of tunnelling impact on flow rates of adjacent extraction water wells. Quart. J. Eng. Geol. Hydrogeol. 53 (2), 236–251.

Hansbo, A., Hansbo, P., 2002. An unfitted finite element method, based on nitsche's method, for elliptic interface problems. Comput. Methods Appl. Mech. Engrg. 191 (47–48), 5537–5552.

HosseiniMehr, M., Cusini, M., Vuik, C., Hajibeygi, H., 2018. Algebraic dynamic multilevel method for embedded discrete fracture model (f-ADM). J. Comput. Phys. 373, 324–345.

Hoteit, H., Firoozabadi, A., 2005. Multicomponent fluid flow by discontinuous Galerkin and mixed methods in unfractured and fractured media. Water Resour. Res. 41, W11412.

Hoteit, H., Firoozabadi, A., 2006. Compositional modeling of discrete-fractured media without transfer functions by the discontinuous Galerkin and mixed methods. SPE J. 11 (03), 341–352.

Hoteit, H., Firoozabadi, A., 2008a. An efficient numerical model for incompressible two-phase flow in fractured media. Adv. Water Resour. 31 (6), 891–905.

Hoteit, H., Firoozabadi, A., 2008b. Numerical modeling of two-phase flow in heterogeneous permeable media with different capillarity pressures. Adv. Water Resour. 31 (1), 56–73.

Huang, H., Long, T.A., Wan, J., Brown, W.P., 2011. On the use of enriched finite element method to model subsurface features in porous media flow problems. Comput. Geosci. 15 (4), 721–736.

Ilinca, F., Hétu, J.-F., 2011. A finite element immersed boundary method for fluid flow around rigid objects. Internat. J. Numer. Methods Fluids 65 (7), 856–875.

Jiang, J., Younis, R.M., 2017a. An improved projection-based embedded discrete fracture model (pEDFM) for multiphase flow in fractured reservoirs. Adv. Water Resour. 109, 267–289.

Jiang, J., Younis, R.M., 2017b. An improved projection-based embedded discrete fracture model (pEDFM) for multiphase flow in fractured reservoirs. Adv. Water Resour. 109, 267–289.

Kadeethum, T., Nick, H., Lee, S., Ballarin, F., 2020. Flow in porous media with low dimensional fractures by employing enriched Galerkin method. Adv. Water Resour. 142, 103620.

Karimi-Fard, M., Durlofsky, L.J., Aziz, K., 2003. An efficient discrete fracture model applicable for general purpose reservoir simulators. In: SPE Reservoir Simulation Symposium. Society of Petroleum Engineers.

Karimi-Fard, M., Firoozabadi, A., 2001. Numerical simulation of water injection in 2D fractured media using discrete-fracture model. In: SPE Annual Technical Conference and Exhibition. Society of Petroleum Engineers.

Keilegavlen, E., Berge, R., Fumagalli, A., Starnoni, M., Stefansson, I., Varela, J., Berre, I., 2021. Porepy: an open-source software for simulation of multiphysics processes in fractured porous media. Comput. Geosci. 25 (1), 243–265.

Kim, J.G., Deo, M.D., 1999, January. Comparison of the performance of a discrete fracture multiphase model with those using conventional methods. In: SPE Reservoir Simulation Symposium. Society of Petroleum Engineers.

Kim, J.G., Deo, M.D., 2000. Finite element, discrete-fracture model for multiphase flow in porous media. AIChE J. 46 (6), 1120–1130.

Köppel, M., Martin, V., Jaffré, J., Roberts, J.E., 2019a. A Lagrange multiplier method for a discrete fracture model for flow in porous media. Comput. Geosci. 23 (2), 239–253.

Köppel, M., Martin, V., Roberts, J.E., 2019b. A stabilized Lagrange multiplier finite-element method for flow in porous media with fractures. GEM-Int. J. Geomath. 10, 7, (2019).

Li, L., Lee, S.H., 2008. Efficient field-scale simulation of black oil in a naturally fractured reservoir through discrete fracture networks and homogenized media. SPE Reserv. Eval. Eng. 11 (04), 750–758.

Lipnikov, K., Manzini, G., Shashkov, M., 2014. Mimetic finite difference method. J. Comput. Phys. 257 (part B), 1163–1227.

Martin, V., Jaffré, J., Roberts, J.E., 2005. Modeling fractures and barriers as interfaces for flow in porous media. SIAM J. Sci. Comput. 26 (5), 1667–1691.

Matthäi, S., Nick, H., Pain, C., Neuweiler, I., 2010. Simulation of solute transport through fractured rock: A higher-order accurate finite-element finite-volume method permitting large time steps. Transp. Porous Media 83, 289–318.

Moinfar, A., 2013. Development of an efficient embedded discrete fracture model for 3D compositional reservoir simulation in fractured reservoirs (Ph.D. Thesis). University of Texas, Austin.

Monteagudo, J.E.P., Firoozabadi, A., 2004. Control-volume method for numerical simulation of two-phase immiscible flow in two-and three-dimensional discrete-fractured media. Water Resour. Res. 40, W07405.

Monteagudo, J.E., Firoozabadi, A., 2007. Control-volume model for simulation of water injection in fractured media: incorporating matrix heterogeneity and reservoir wettability effects. SPE J. 12 (03), 355–366.

Moortgat, J., Amooie, M.A., Soltanian, M.R., 2016. Implicit finite volume and discontinuous Galerkin methods for multicomponent flow in unstructured 3D fractured porous media. Adv. Water Resour. 96, 389–404.

Moortgat, J., Firoozabadi, A., 2013a. Higher-order compositional modeling of three-phase flow in 3D fractured porous media based on cross-flow equilibrium. J. Comput. Phys. 250, 425–445.

Moortgat, J.B., Firoozabadi, A., 2013b. Three-phase compositional modeling with capillarity in heterogeneous and fractured media. SPE J. 18 (06), 1–150.

Nikitin, K.D., Yanbarisov, R.M., 2020. Monotone embedded discrete fractures method for flows in porous media. J. Comput. Appl. Math. 364, 112353, 15.

Noorishad, J., Mehran, M., 1982. An upstream finite element method for solution of transient transport equation in fractured porous media. Water Resour. Res. 18 (3), 588–596.

Nordbotten, J.M., Boon, W.M., Fumagalli, A., Keilegavlen, E., 2019. Unified approach to discretization of flow in fractured porous media. Comput. Geosci. 23 (2), 225–237.

Odsæter, L.H., Kvamsdal, T., Larson, M.G., 2019. A simple embedded discrete fracture–matrix model for a coupled flow and transport problem in porous media. Comput. Methods Appl. Mech. Engrg. 343, 572–601.

Olorode, O., Wang, B., Rashid, H.U., 2020. Three-dimensional projection-based embedded discrete-fracture model for compositional simulation of fractured reservoirs. SPE J..

Raviart, P.-A., Thomas, J.M., 1977. A mixed finite element method for 2nd order elliptic problems. In: Mathematical Aspects of Finite Element Methods (Proc. Conf., Consiglio Naz. Delle Ricerche (C.N.R.), Rome, 1975). In: Lecture Notes in Math., vol. 606, pp. 292–315.

Reichenberger, V., Jakobs, H., Bastian, P., Helmig, R., 2006. A mixed-dimensional finite volume method for two-phase flow in fractured porous media. Adv. Water Resour. 29 (7), 1020–1036.

Salimzadeh, S., Khalili, N., 2015. Fully coupled XFEM model for flow and deformation in fractured porous media with explicit fracture flow. Int. J. Geomech. 16 (4), 04015091.

Sandve, T.H., Berre, I., Nordbotten, J.M., 2012. An efficient multi-point flux approximation method for discrete fracture–matrix simulations. J. Comput. Phys. 231 (9), 3784–3800.

Schädle, P., Zulian, P., Vogler, D., Bhopalam, S.R., Nestola, M.G., Ebigbo, A., Krause, R., Saar, M.O., 2019. 3D Non-conforming mesh model for flow in fractured porous media using Lagrange multipliers. Comput. Geosci. 132, 42–55.

Schöberl, J., 2014. C++11 Implementation of Finite Elements in NGSolve. ASC Report 30/2014, Institute for Analysis and Scientific Computing, Vienna University of Technology.

Schwenck, N., 2015. An XFEM-Based Model for Fluid Flow in Fractured Porous Media (Ph.D. Thesis). Universität Stuttgart.

Ski, S.N.P.I., 1987. The International Hydrocoin Project- Background and Results. Organization for Economic Co-operation and Development, Paris, France.

Tene, M., Bosma, S., Al Kobaisi, M., Hajibeygi, H., 2017. Projection-based embedded discrete fracture model (pEDFM). Adv. Water Resour. 105, 205–216.

Vasilyeva, M., Babaei, M., Chung, E., Spiridonov, D., 2019. Multiscale modeling of heat and mass transfer in fractured media for enhanced geothermal systems applications. Appl. Math. Model. 67, 159–178.

Warren, J.E., Root, P.J., 1963. The behavior of naturally fractured reservoirs. Soc. Pet. Eng. J. 3, 245–255.

Xu, Z., Huang, Z., Yang, Y., 2021. The hybrid-dimensional Darcy's law: A reinterpreted discrete fracture model for fracture and barrier networks on non-conforming meshes.

Xu, J., Sun, B., Chen, B., 2019. A hybrid embedded discrete fracture model for simulating tight porous media with complex fracture systems. J. Pet. Sci. Eng. 174, 131–143.

Xu, Z., Yang, Y., 2020. The hybrid dimensional representation of permeability tensor: A reinterpretation of the discrete fracture model and its extension on nonconforming meshes. J. Comput. Phys. 415, 109523.

Yan, X., Huang, Z., Yao, J., Li, Y., Fan, D., 2016. An efficient embedded discrete fracture model based on mimetic finite difference method. J. Pet. Sci. Eng. 145, 11–21.

Zhang, N., Yao, J., Huang, Z., Wang, Y., 2013. Accurate multiscale finite element method for numerical simulation of two-phase flow in fractured media using discrete-fracture model. J. Comput. Phys. 242, 420–438.

Zhang, R.H., Zhang, L.H., Luo, J.X., Yang, Z.D., Xu, M.Y., 2016. Numerical simulation of water flooding in natural fractured reservoirs based on control volume finite element method. J. Pet. Sci. Eng. 146, 1211–1225.

Zidane, A., Firoozabadi, A., 2014. An efficient numerical model for multicomponent compressible flow in fractured porous media. Adv. Water Resour. 74, 127–147.